On the evolution of the size of Lyman alpha haloes across cosmic time: no change in the circumgalactic gas distribution when probed by line emission

Axel Runnholm, Matthew J. Hayes, Yu-Heng Lin, Jens Melinder, Claudia Scarlata, Angela Adamo, Ramona Augustin, Arjan Bik, Jérémy Blaizot, John M. Cannon, et al.

Monthly Notices of the ROYAL ASTRONOMICAL SOCIETY

MNRAS **522,** 4275–4293 (2023) https://doi.org/10.1093/mnras/stad1264
Advance Access publication 2023 April 27

On the evolution of the size of Lyman alpha haloes across cosmic time: no change in the circumgalactic gas distribution when probed by line emission

Axel Runnholm [1★] Matthew J. Hayes [1] Yu-Heng Lin [2] Jens Melinder,[1] Claudia Scarlata [2] Angela Adamo,[1] Ramona Augustin [3] Arjan Bik,[1] Jérémy Blaizot,[4] John M. Cannon,[5] Sebastiano Cantalupo [6,7] Thibault Garel,[8] Max Gronke [9] Edmund C. Herenz,[10] Floriane Leclercq [11] Göran Östlin,[1] Celine Peroux [12,13] Armin Rasekh,[1] Michael J. Rutkowski,[14] Anne Verhamme[8] and Lutz Wisotzki[15]

[1]*Department of Astronomy, Oscar Klein Centre, Stockholm University, AlbaNova universitetscentrum, SE-106 91 Stockholm, Sweden*
[2]*Minnesota Institute for Astrophysics, School of Physics and Astronomy, University of Minnesota, 316 Church str SE, Minneapolis, MN 55455,USA*
[3]*Space Telescope Science Institute, 3700 San Martin Drive, Baltimore, MD, 21218, USA*
[4]*Univ Lyon, Univ Lyon1, Ens de Lyon, CNRS, Centre de Recherche Astrophysique de Lyon UMR5574, F-69230, Saint-Genis-Laval, France*
[5]*Department of Physics and Astronomy, Macalester College, 1600 Grand Avenue, Saint Paul, MN 55105, USA*
[6]*Dipartimento di Fisica, Universitá di Milano Bicocca, Piazza della Scienza 3, I-20126 Milano, Italy*
[7]*Institute for Astronomy, ETH Zurich, CH-8093 Zurich, Switzerland*
[8]*Department of Astronomy, University of Geneva, Chemin Pegasi 51, CH-1290 Versoix, Switzerland*
[9]*Max Planck Institut fur Astrophysik, Karl-Schwarzschild-Straße 1, D-85748 Garching bei München, Germany*
[10]*European Southern Observatory, Av. Alonso de Córdova 3107, 763 0355 Vitacura, Santiago, Chile*
[11]*Department of Astronomy, The University of Texas at Austin, 2515 Speedway, Stop C1400, Austin, TX 78712, USA*
[12]*European Southern Observatory, Karl-Schwarzschildstrasse 2, D-85748 Garching bei München, Germany*
[13]*Aix Marseille Université, CNRS, LAM (Laboratoire d'Astrophysique de Marseille) UMR 7326, F-13388 Marseille, France*
[14]*Department of Physics and Astronomy, Minnesota State University, Mankato, MN 56001, USA*
[15]*Leibniz-Institut für Astrophysik Potsdam (AIP), An der Sternwarte 16, D-14482 Potsdam, Germany*

Accepted 2023 April 24. Received 2023 April 20; in original form 2022 May 25

ABSTRACT

Lyman α (Lyα) is now routinely used as a tool for studying high-redshift galaxies, and its resonant nature means it can trace neutral hydrogen around star-forming galaxies. Integral field spectrograph measurements of high-redshift Lyα emitters indicate that significant extended Lyα halo emission is ubiquitous around such objects. We present a sample of redshift 0.23 to 0.31 galaxies observed with the *Hubble Space Telescope* selected to match the star formation properties of high-z samples while optimizing the observations for detection of low surface brightness Lyα emission. The Lyα escape fractions range between 0.7 and 37 per cent, and we detect extended Lyα emission around six out of seven targets. We find Lyα halo to UV scale length ratios around 6:1, which is marginally lower than high-redshift observations, and halo flux fractions between 60 and 85 per cent – consistent with high-redshift observations – when using comparable methods. However, our targets show additional extended stellar UV emission: we parametrize this with a new double exponential model. We find that this parametrization does not strongly affect the observed Lyα halo fractions. We find that deeper Hα data would be required to firmly determine the origin of Lyα halo emission; however, there are indications that Hα is more extended than the central FUV profile, potentially indicating conditions favourable for the escape of ionizing radiation. We discuss our results in the context of high-redshift galaxies, cosmological simulations, evolutionary studies of the circumgalactic medium in emission, and the emission of ionizing radiation.

Key words: galaxies: haloes – galaxies: starburst.

1 INTRODUCTION

Lyman α (Lyα) results from the transition from the 2p to 1s energy levels of hydrogen and under normal gas conditions, 68 per cent of ionizing photons are processed through this transition (Dijkstra 2019). This, coupled with the prevalence of hydrogen gas in galaxies, means that it is intrinsically the strongest emission line in star-forming systems. However, since this transition is from the ground state of hydrogen, most astrophysical media containing even small amounts of neutral hydrogen are optically thick to Lyα.

The resonant nature of the Lyα transition means that Lyα-photons absorbed by hydrogen are re-emitted in that same transition and scatter on neutral hydrogen. This has the interesting and very

★ E-mail: axel.runnholm@astro.su.se

important consequence that some properties of the gas in an emitting galaxy can be encoded in the Lyα radiation.

If we can understand how the spatial profiles of Lyα relate to the properties of the galaxy as a whole, it could improve our understanding of how neutral gas is distributed in and around such systems. Since Lyα is in many cases very bright, we can potentially spatially map neutral hydrogen at much larger redshifts than what is practically observable using direct tracers such as 21-cm emission (see, e.g. Obreschkow, Heywood & Rawlings 2011). This is especially interesting for studying the circumgalactic (CGM) and intergalactic media (IGM). This tenuous gas can typically only be studied on fortuitous sightlines where the CGM is intersected by a bright background continuum source. Lyα imaging, on the other hand, could be used to map the distribution of gas around an individual galaxy.

This idea was first explored using narrowband imaging of Lyman Break Galaxies (LBGs) by Steidel et al. (2011), where stacking of sources allowed detection of low surface brightness emission. These results indicated significant and very extended Lyα emission around the median stack with a characteristic scale length of 25 kpc. More recent results using integral field spectrographs (IFSs), such as the Multi-Unit Spectroscopic Explorer (MUSE; Bacon et al. 2010) on the Very Large Telescope (VLT) and the Keck Cosmic Web Imager (KCWI; Morrissey et al. 2018) on Keck, have clearly detected Lyα halo emission around high-z galaxies. Using sensitive IFSs allows the detection of individual haloes (see e.g. Erb, Steidel & Chen 2018). These haloes are indeed very extended, with exponential scale lengths between 1 and 18 kpc with a median around 4.5 kpc (Wisotzki et al. 2016; Leclercq et al. 2017, 2020), which is much larger than the detected UV emission of these galaxies. Kusakabe et al. (2022) studied Lyα emission around UV selected galaxies, also using MUSE, and found an incidence rate of 80 per cent and that the haloes extend as far as 40 kpc. Scale lengths similar to the MUSE results have also been found in narrowband studies, including one subsample of Feldmeier et al. (2013) and the results of Momose et al. (2014, 2016). Chen et al. (2021) used KCWI and found more extended Lyα-haloes with a scale length of the median stack of 17.5 kpc, more similar to the LBGs studied by Steidel et al. (2011). Niemeyer et al. (2022) present the median-stacked Lyα surface brightness profiles of 968 spectroscopically selected Lyα emitting galaxies (LAEs) at redshifts $1.9 < z < 3.5$ in the early data of the Hobby–Eberly Telescope Dark Energy Experiment (HETDEX). They find that the median-stacked radial profile at $r < 80$ kpc agrees with the results from the MUSE sample, but is more extended at $r > 80$ kpc. These instruments have opened up a new frontier of research where we can not only study individual Lyα haloes, but samples of individual halo detections can become large enough for population statistics to be derived.

Despite the ease with which such high-z surveys can be conducted, they remain fundamentally limited by the lack of ancillary data, such as rest-frame optical spectroscopy and high-resolution imaging of the stellar population, that can be used to infer the properties of the systems that give rise to the Lyα haloes. In order to study the origin of Lyα haloes and the properties of their host galaxies, we need to turn to observations in the low redshift universe.

However, studying Lyα at low redshift is challenging – primarily because the UV wavelength of Lyα requires space based observations. Early low redshift studies such as Kunth et al. (2003), Hayes et al. (2005, 2007), and Östlin et al. (2009) used a Lyα transmitting narrowband filter on the Solar Blind Channel (SBC) on the *Hubble Space Telescope* (*HST*) Advanced Camera for Surveys (ACS). However, Hayes et al. (2009) showed that synthesizing narrow-band observations from adjacent long pass broad-band observations was more effective. The Lyman Alpha Reference Sample (LARS; Hayes et al. 2014; Östlin et al. 2014) has successfully used this method to image Lyα, and has shown that there are significant differences in the morphologies of Lyα compared to those of Hα and UV. The high spatial resolution of LARS enables the study of small structural differences and has shown, for instance, that knots and structures present in UV and Hα are absent in Lyα and that the Lyα structure, in general, appears smoother (Bridge et al. 2017). The centroids of Lyα emission and its position angle also significantly differ from the stellar UV emission (Rasekh et al. 2021).

LARS, which consists of galaxies at redshift $\lesssim$0.2 has confirmed significant Lyα haloes extending 1 to 4 times further than both Hα and stellar far UV (FUV; Hayes et al. 2013; Rasekh et al. 2021). Yang et al. (2017) used a different technique based on COS acquisition images and found very similar ratios with Lyα extending 2–4 times further than the UV. There is some indication that high-redshift galaxies such as those observed by Leclercq et al. (2017) have larger ratios than this, hinting that there may be some redshift evolution in halo sizes. However, neither Wisotzki et al. (2016) nor Leclercq et al. (2017) see any redshift evolution within their samples despite the significant redshift range (between $z \sim 3$ and 6.6) it covers. It is important to note; however, that this redshift range corresponds to only 1.3 Gyr, in contrast to the $\sim$11 Gyr that elapses between $z = 3$ and 0.

Determining whether there is a change in halo sizes between low and high z is crucial for understanding galaxy evolution, since it would imply a significant physical evolution in the properties of Lyα-halo-hosting galaxies over this time. Absorption line studies, such as COS-Haloes (Tumlinson et al. 2013), COS-GASS (Borthakur et al. 2015), and COS-Bursts (Heckman et al. 2017), have shown that the atomic gas haloes of star forming galaxies extend far beyond the stellar components with absorption equivalent widths (EWs) higher than 0.1 Å (corresponding to gas column densities $\gtrsim 10^{17}$, which, for normal gas temperatures, implies $\tau \gtrsim 1000$ for Lyα) as far as 300 kpc from the central galaxy. This appears to hold regardless of viewing angles of the galaxies, indicating a covering fraction of 1 for this neutral medium. The CGM of $z \approx 0$ galaxies therefore does have sufficient HI in their haloes to scatter Lyα out to large distances, and yet the observed Lyα emission around individual galaxies declines significantly faster than the neutral gas column does.

LARS is optimized to study the detailed structural differences between FUV, Hα, and Lyα, and therefore selects very low redshift targets to get the best possible spatial resolution. The field of view (FoV) corresponds to $\sim$10 kpc at the redshift of LARS (Rasekh et al. 2021). This means that the observations cannot cover radii that come even close to those probed by the absorption line studies mentioned above and can only probe $\sim$2 scale lengths of a median Lyα halo ($\sim$4.5 kpc) found in Leclercq et al. (2017). Consequently, the observations are more optimized to characterize the detailed morphology of the Lyα emission and absorption rather than the low surface brightness extent of them. In order to probe larger scales, and definitively determine whether Lyα haloes evolve between $z \sim 0$ and 3, a larger FoV is required. Therefore, we designed an *HST* program for doing LARS type imaging at $0.23 \leq z \leq 0.31$, where we can obtain such observations with minimal background from geocoronal emission. In this work we present the results of this *HST* program.

The paper is structured as follows: in Section 2, we present the data set and the details of our *HST* observations. In Section 3, we discuss the methodology, with particular focus spent on the data reduction and production of Lyα images. In Section 4, we present and discuss the primary results from the Lyα imaging and in Section 4.2, we give detailed descriptions of the objects in this study. Finally, we

Table 1. The sample of galaxies.

Galaxy	Short name	RA*	Dec*	Redshift
SDSSJ0004−1011	J0004	00 04 30.3	−10 11 29.6	0.2386
SDSSJ0139+0108	J0139	01 39 13.2	+01 08 56.0	0.3073
SDSSJ0156−0101	J0156	01 56 55.8	−01 01 16.5	0.2696
SDSSJ0232−0048	J0232	02 32 43.6	−00 48 32.3	0.3095
SDSSJ2318−0041	J2318	23 18 13.0	−00 41 26.0	0.2517
SDSSJ2353+0231	J2353	23 53 35.5	+02 31 50.2	0.2333
SDSSJ2359+0108	J2359	23 59 26.7	+01 08 38.8	0.2607

* RA and Dec are in J2000

discuss the potential implications of our findings in Section 5 and conclude in Section 6. We assume a flat ΛCDM cosmology with $H_0 = 70\,\mathrm{kms}^{-1}\,\mathrm{Mpc}^{-1}$, $\Omega_m = 0.3$, $\Omega_\Lambda = 0.7$.

2 DATA

We obtained *HST* imaging observations in six bands of seven galaxies at redshifts $0.23 \leq z \leq 0.31$ (see Table 1 for details) taken as part of GO 15643, PI Hayes. Throughout the paper, we will refer to the targets using the short names introduced in this table. *HST*/COS spectral observations of these targets will be presented in a future paper. The *HST* filters included two UV filters in the Solar Blind Channel (SBC) of ACS (*F*150*LP* and *F*165*LP*), that were selected to enable synthetic Lyα narrow-band observations (see Section 3.2.2 for details on the continuum subtraction of the Lyα images). In addition, we used three optical filters in the Wide Field Channel of ACS (WFC; *F*435*W*, *F*555*W*, *F*814*W*) and a narrow-band (*FR*782*N* or *FR*853*N* depending on redshift) to capture Hα, also in ACS/WFC. The observations are summarized in Table 2, and optical composites showing the morphologies of the targets are displayed in Fig. 1.

2.1 Sample selection

We select objects with redshift such that Lyα falls in the *F*150*LP* but not the *F*165*LP* filter. This limits the redshift range to $0.23 < z < 0.31$. Compared to most previous studies, this filter combination ensures that no strong skylines, specifically OI at 1305 and 1356 Å, are transmitted by the filters. Over this redshift range, the ACS/SBC detector covers a physical distance in excess of ≈60 kpc. This ensures that there is sufficient space in the frame to subtract any remaining background from the image while being confident that no Lyα signal is lost in the process.

Sources were selected from a catalogue of re-fitted SDSS DR 14 (Abolfathi et al. 2018) spectra according to the following criteria:

(i) Less than 0.2 mag *u*-band extinction from the Milky Way

(ii) Declination below +5° to ensure visibility from Cerro Paranal to enable further follow-up studies

(iii) Full width at half maximum (FWHM) of the optical emission lines less than 250 km s^{-1}, and a position in the BPT diagram below the Kauffmann et al. (2003) demarcation line in order to ensure that contamination from AGN was kept to a minimum

(iv) Far UV absolute magnitude M_{FUV} in the range −17.5 to −22 from GALEX (Martin et al. 2003) in order to overlap with high-redshift galaxies. Specifically, the lower end was selected to match the 25th percentile of Leclercq et al. (2017) and the upper end was selected to match the upper brightness limit of Steidel et al. (2011).

(v) Hα equivalent width larger than 100 Å in order to ensure that all galaxies produce significant Lyα. This also enables a direct comparison between this sample of galaxies and the LARS sample at lower redshift.

After these criteria were applied, there were still more than 200 galaxies that could be included in the sample. The seven galaxies were then selected to span the full range of galaxy properties in terms of position on the star-forming main sequence, BPT diagram, and UV slope versus Hα equivalent width (see Fig. 2).

In the first panel of Fig. 2, the dashed line shows the star forming main sequence at redshift ∼2 from Daddi et al. (2007) and our seven galaxies lie close to and in general above that relation, demonstrating that they are, at least in this respect, comparable to high-redshift galaxies.

3 METHODS

3.1 Observations and data reduction

The total exposure times and filters used are summarized in Table 2. The observations were performed with a custom calculated large (∼3 arcsec) dithering pattern specially designed to minimize flat field uncertainties and biases, as well as allow for subpixel sampling of the PSF.

3.1.1 UV data

The individual UV exposures (from the ACS/SBC) were initially reduced using the CALACS pipeline with the latest calibration files to produce flatfield-corrected (FLT) frames. We implemented an additional, custom step to correct for residual dark-current in the SBC detector. This dark current is strongly temperature dependent and therefore varies between exposures and time on orbit. The procedure used a collection of dark-current images taken at various times and

Table 2. *HST* exposure times in seconds.

Bandpass alias *HST* Instrument *HST* Filter name Galaxy	Lyα ACS/SBC *F*150*LP*	FUV continuum ACS/SBC *F*165*LP*	U* ACS/WFC *F*435*W*	B* ACS/WFC *F*555*W*	I* ACS/WFC *F*814*W*	Hα ACS/WFC
J0004	5104	7698	1132	1030	800	1300 (FR782N)
J0139	5168	7600	1116	1016	778	1300 (FR853N)
J0156	5088	7680	1116	1016	778	1300 (FR853N)
J0232	5108	7660	1116	1016	778	1300 (FR853N)
J2318	5150	7751	1116	1016	778	1300 (FR853N)
J2353	5090	7678	1128	1026	794	1300 (FR782N)
J2359	5078	7690	1116	1016	778	1300 (FR853N)

* These aliases refer to the approximate restframe bandpasses.

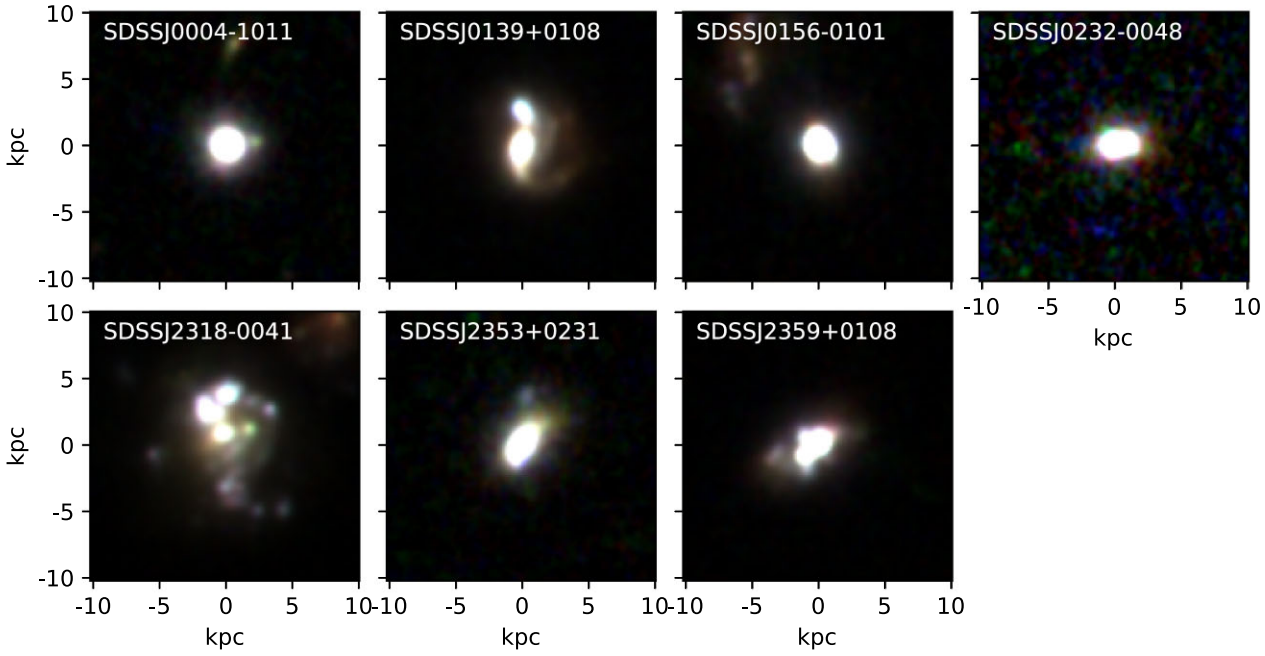

Figure 1. Optical three-colour composite images of the seven targets. Filter set-up: Red – *F*814*W*, Green – *F*555*W*, Blue – *F*435*W*.

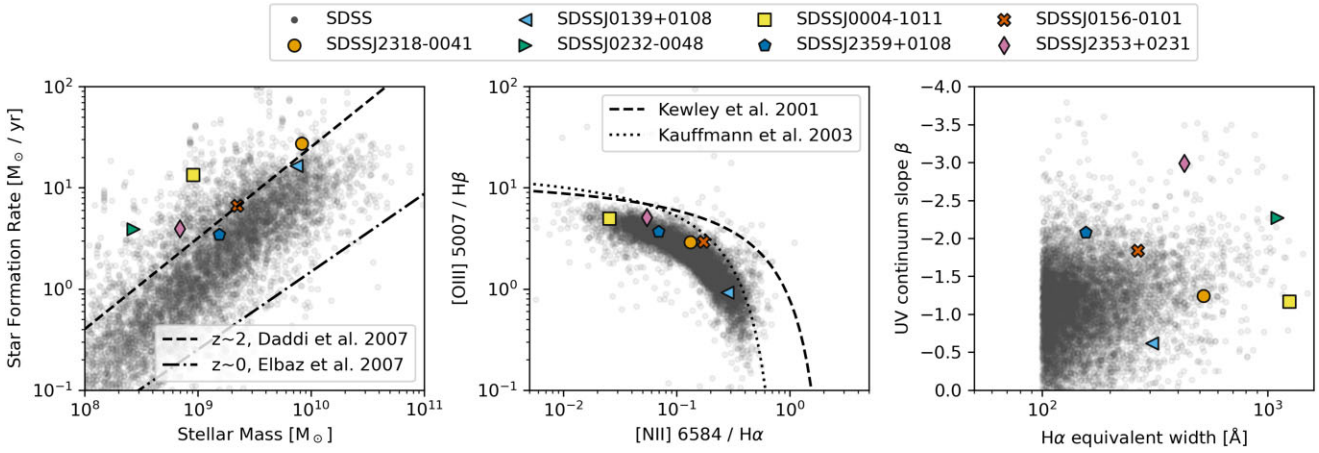

Figure 2. Sample selection figures. The left-hand panel shows star formation rate against stellar mass. The black points show a sample of 7000 SDSS galaxies with the single selection criterion of having a high ($\geq$100 Å) Hα equivalent width. The dash–dotted line shows the star-forming main sequence relation at redshift $\sim$0 derived from the SDSS from Elbaz et al. (2007) and the dashed line shows the main sequence at redshift 2 from Daddi et al. (2007). The central panel shows the BPT diagram (Baldwin, Phillips & Terlevich 1981) with the relations from Kewley et al. (2001) and Kauffmann et al. (2003) showing the demarcation between star forming galaxies and AGN. The third panel shows the UV slope β (assuming the standard proportionality $f_\lambda \propto \lambda^\beta$) derived from *GALEX* photometry against the Hα equivalent width.

Table 3. Measured optical line fluxes.

Galaxy	Hα	Hβ	Hγ	[O III]$_{5007}$	[O III]$_{4363}$	[O II]$_{3726,\,3729}$	[N II]$_{6584}$	[S II]$_{6717}$
J0004	1420 ± 90	490 ± 31	245 ± 19	2440 ± 188	70 ± 7	740 ± 50	36 ± 6	57 ± 6
J0139	990 ± 130	345 ± 45	170 ± 30	320 ± 50	14 ± 13	1100 ± 175	280 ± 30	165 ± 33
J0156	535 ± 54	187 ± 19	88 ± 12	550 ± 60	7.5 ± 2	520 ± 60	92 ± 9	60 ± 6
J0232	230 ± 40	80 ± 13	38 ± 8	490 ± 91	11 ± 3	102 ± 18	0.8 ± 3.6	6.4 ± 2.4
J2318	2600 ± 100	900 ± 34	410 ± 23	2600 ± 116	31 ± 9	3000 ± 130	340 ± 12	295 ± 11
J2353	440 ± 93	154 ± 32	63 ± 17	785 ± 175	6.6 ± 2.8	330 ± 76	24 ± 5	24 ± 6.7
J2359	300 ± 35	105 ± 12	47 ± 9	388 ± 53	7 ± 4	390 ± 55	21 ± 8	40 ± 8

>All fluxes are given in units of 10^{-17} erg s^{-1} cm^{-2} and corrected for foreground and internal dust extinction.

temperatures, and fitted the dark-current image to each SBC frame with χ^2 minimization of the form

$$B = A \times I_{\rm DC} + C, \quad (1)$$

where B is the total fitted background, A is the amplitude which is allowed to vary, $I_{\rm DC}$ is a given dark-current image, and C is a constant that represents the actual contribution of the (flat) sky background. The best-fit background and dark-current were then subtracted from each FLT frame.

This procedure works very well for all of the data that was taken as a part of GO 15643. However, two of our *F*150*LP* exposures are archival data taken as a part of GO 11107 (PI Heckman), and these images showed an additional background gradient after the dark-current subtraction. In these cases, we mask the edges of the image as well as the source itself by selecting a broad circular annulus centred on the galaxy and fit an additional plane to the flux in this region, which is then subtracted.

3.1.2 *Optical data*

The optical data (from ACS/WFC) were pipeline-processed in the same manner as the UV data. Since each optical filter only contains two exposures, we found that drizzling could not adequately remove all cosmic rays from the frames. We therefore did a separate cosmic ray rejection on the frames using the `astroscrappy` tool (McCully et al. 2018), which is based on `lacosmic` (van Dokkum 2001) before drizzling.

The Hα narrow-band images were taken using tunable ramp filters. This allows us to centre the band on the Hα line, but those filters do not cover the whole chip. This means that standard `astrodrizzle` background estimates are inaccurate. We therefore instead fit and subtract the background of the unvignetted region using a flat plane in the same way as was done for the GO 11 107 UV images.

3.1.3 *Image alignment*

After the pipeline reduction and dark-current subtraction, we performed fine-alignment of the images. Due to the lack of stars in the fields, especially in the FUV filters, this could not be done using the standard `TweakReg` task from `astrodrizzle`. We therefore developed a custom cross-correlation based alignment routine.

The first step was to make sure that all exposures taken with a given filter were well aligned with each other. For the optical filters, only one *HST* visit with two individual exposures was used, which meant that the default pipeline World Coordinate Systems (WCS) were in general well matched. In two visits, however, this was not the case: *F*555*W* for J0139 and FR853N for J2359. These were treated according to the methodology developed for the UV filters (see below).

For the UV filters, there were three individual visits per galaxy per filter, and in most cases, even the fine alignment of exposures belonging to the same visit was poor (offsets $\gg$1 px). We therefore had to align all exposures in each filter with each other. This was done as follows:

(i) Each exposure was individually drizzled to ensure that all images had the same pixel scale and were derotated. We used a pixel scale of 0.″01 at this stage to ensure that alignment could be done on a subpixel level compared to the final pixel scale (0.″04).

(ii) The exposures were then compared to each other using a two-dimensional correlation analysis (using `scipy.signal.2dcorrelation`), and the point of maximum correlation was converted into a pixel shift.

(iii) These pixel shifts were then converted into right ascension and declination, and added as a shift to the WCS of the original images.

The philosophy of this approach is to mimic that of `tweakreg` in `astrodrizzle`, which minimizes the number of times pixel data are resampled, compared to manual realignment and regridding post-drizzle, and to maximize the correlation of signal between pixels in the final images. For J0139 and J0232, the individual *F*165*LP* exposures had insufficient signal-to-noise to produce stable correlation analysis. In these cases, we instead drizzled the exposures from each visit together. These visit-level drizzles were then aligned with each other as described above.

We then drizzle each filter together, producing a total 1 frame per filter, again using a small pixel size of 0.01 arcsec. These frames are then used as input to an inter filter correlation analysis, where the *F*435*W* frame is used as the reference. Again, the resulting shifts are converted to ΔRA and ΔDec and added to the WCS of the original frames. This alignment process results in six individual drizzled images that are aligned onto a common grid with consistent world-coordinate systems. The final pixel scale used was 0.″04.

3.1.4 *Re-estimating the UV uncertainties*

A simple comparison between the RMS values in the sky regions of the final drizzled image and compared to the median of the errors given in the weight frame produced by drizzle indicated that the drizzle errors were significant overestimates of the true standard deviations, by factors of up to 10. We therefore re-estimate the error as the quadrature sum of a constant RMS estimated from the sky regions of the frame and the square root of the signal (counts) in the frame. Additionally, the drizzling means that the noise in the image is correlated. We therefore use the correction factor given in Fruchter & Hook (2002) to correct for this:

$$R = \frac{1}{1 - \frac{1}{3r}}, \quad (2)$$

where $r = \text{pixfrac scale}^{-1}$ and the pixfrac is set to 1 in this case. This expression is valid for a filled uniform dither. Our observations were designed for this to be a reasonable approximation. Within each visit, there were several dithering positions taken, and each one was designed to reconstruct the PSF with 1/3 pixel dithers in x and y.

3.1.5 *PSF matching*

The point spread functions (PSF) of the *HST* cameras varies strongly between the ACS/SBC and the ACS/WFC, and also between the different filters in each camera. After the images are aligned, we then match images obtained in each filter to a common PSF because our modelling requires spectral analysis to be performed at the level of individual pixels.

For the optical filters, we construct PSFs based on TinyTim modelling (Krist, Hook & Stoehr 2011). The raw PSF models from TinyTim are added to the individual science frames and the final models are then extracted from the inserted PSFs in the drizzled and stacked images. For WFC data, where the spatial variance of the PSF does not need to be taken into account, TinyTim provides an accurate characterization of the PSF, however the situation is more complex for the ACS SBC. The PSF of this instrument is characterized by a narrow core and strong wings, which are not captured in the

TinyTim models. See, for instance, Hayes et al. (2016) and Melinder et al. (2023) for an extensive discussion of this. For this reason we have created a fully empirical PSF model for the SBC filters based on observations of single stars in the globular cluster NGC 6681. Based on the models of the individual PSFs, we make and apply a convolution kernel that homogenizes the images.

3.1.6 Voronoi binning

To ensure sufficient signal-to-noise for SED-fitting (which we use to model the continuum in the Lyα transmitting filter, see Section 3.2.2), the data were binned using a Voronoi tesselation algorithm. The algorithm used was the Weighted Voronoi Tesselation (Diehl & Statler 2006) with the FUV image as a reference. The target signal-to-noise was 5 and the maximum bin size was set to 50 pixels (0.08 arcsec^2).

3.1.7 Final background subtraction

Since we are interested in very low surface brightness emission, the quality of the background subtraction is crucial. Therefore, as a final step of the data reduction, we evaluated and removed any residual background in the drizzled images. We masked the data by selecting a wide annulus around the galaxies and fitted a plane, which was then subtracted from the image, leaving a flat background centred on zero.

3.2 Data analysis

3.2.1 Continuum subtracting Hα

In order to get a line-map of Hα emission, we need to subtract the stellar continuum contribution from the narrow-band observations, which we do by using the following expression (Hayes & Östlin 2006):

$$F_{\rm line} = \frac{W_{\rm b}F_{\rm n} - W_{\rm n}F_{\rm b}}{W_{\rm b}W_{\rm n}}, \tag{3}$$

where $F_{\rm b}$ and $W_{\rm b}$ are the flux and width of the broad-band – *F*814*W*, $F_{\rm n}$, and $W_{\rm n}$ are the flux and width of the narrow-band. $W_{\rm b}$ is taken to be 1260.3 Å from the instrument manual. For the narrow-band, we calculate the width based on the expression given in Bohlin & Tsvetanov (2000). We also estimate the uncertainties in this Hα frame using a 500-iteration Monte Carlo simulation, where we randomize the broad-band and narrow-band fluxes based on their error frames.

3.2.2 Modelling the UV continuum

To estimate the stellar continuum at the wavelength of Lyα, we use the `Lyman Alpha eXtraction Software` (`LaXs`; Hayes et al. 2009), the latest version of which is presented in detail in Melinder et al. (2023). For completeness, we provide a summary of the modelling steps below:

`LaXs` models the SED in each pixel, or in this case, Voronoi cell, and uses the models to estimate the continuum at Lyα. The input to `LaXs` is therefore a set of images from all of our *HST* bands that have been drizzled to the same pixel scale and PSF matched. It then models the SED for each pixel. The SED model fits two stellar populations, one young and one old, and a dust extinction. The age of the old population is kept fixed at 1 Gyr, whereas age of the young population is allowed to vary between 1 and 100 Myr. The stellar population spectra are taken from the spectral synthesis code Starburst99 (Leitherer et al. 1999) and are matched to the nebular metallicity of the galaxy, as measured by the O3N2 metallicity indicator (Marino et al. 2013, see Table 4), as closely as possible without interpolating between models. For these fits, we also need to select a dust attenuation law – on the basis of the low metallicities and dwarf nature of our galaxies, we opt for the SMC dust attenuation law (Prevot et al. 1984) in all cases. The SED fit is used to calculate a pixel-by-pixel scaling factor that is then applied to the FUV image to create the continuum map at the wavelength sampled by the *F*150*LP* filter. This estimated continuum is then subtracted from the *F*150*LP* image to create the final Lyα image.

Table 4. Properties derived from the SDSS spectra.

Galaxy	$E(B-V)$[mag]	O32	12 + log(O/H)	N2 index
J0004	0.14 ± 0.02	3.3 ± 5.7	8.04 ± 0.02	0.026 ± 0.004
J0139	0.39 ± 0.04	0.28 ± 0.09	8.42 ± 0.02	0.28 ± 0.03
J0156	0.09 ± 0.03	1 ± 0.74	8.27 ± 0.02	0.17 ± 0.017
J0232	0.1 ± 0.06	4 ± 24	7.84 ± 0.42	0.003 ± 0.016
J2318	0.18 ± 0.01	0.9 ± 0.2	8.25 ± 0.01	0.132 ± 0.005
J2353	0.03 ± 0.06	2.4 ± 7.8	8.11 ± 0.04	0.05 ± 0.01
J2359	0.13 ± 0.04	1 ± 0.8	8.16 ± 0.04	0.07 ± 0.03

We use a 500-realization Monte Carlo (MC) simulation to estimate the statistical errors in each pixel of the resulting Lyα images. In each iteration, the input images are perturbed according to their error frames, and the fits are rerun. The full set of results of the MC are saved as a datacube, which we use to estimate errors in our measurements (See Section 4.1 and Section 3.2.4 for specifics).

In our case, we give `LaXs` four continuum bands to fit: *F*165*LP*, *F*435*W*, *F*555*W*, and *F*814*W*. However, the *F*814*W* also contains a contribution from the Hα line. Therefore, we first use the following companion result to equation (3) to calculate the line-corrected continuum flux density

$$f_{\rm cont} = \frac{F_{\rm b} - F_{\rm n}}{W_{\rm b} - W_{\rm n}}. \tag{4}$$

The line-corrected *F*814*W* image is then used in the SED fit in place of the standard *F*814*W* data.

The ramp filters in ACS/WFC also transmit the [N II] $\lambda\lambda$6548, 6584 Å doublet. We correct for this contamination in a global sense using the spectroscopically measured [N II] to Hα line ratio (N2 index, see Section 3.2.3).

3.2.3 Optical spectroscopy

To measure the optical spectroscopic properties of our galaxies, we downloaded the SDSS optical spectra and reanalysed them. The fitting code that we use simultaneously measures the fluxes of 18 optical lines that are constrained to have a common redshift, i.e. centroid shift. The code also takes into account the varying spectral resolution of the SDSS spectrograph by linearly interpolating the spectroscopic resolving power *R*, which varies from 1600 at ∼3000 Å to 3500 at ∼9000 Å. The full linewidth of the spectral lines is then taken as a convolution of the width from the spectrograph and an intrinsic linewidth, which is fitted for and kept common for all lines.

We correct our linefluxes for dust absorption using the `PyNeb` (Luridiana, Morisset & Shaw 2015) reddening correction module. We correct for both Milky Way extinction and internal dust attenuation using the CCM89 law (Cardelli, Clayton & Mathis 1989). Note that when describing the SED fit to the stellar continuum above (Section 3.2.2), we used the SMC extinction law – the reason for

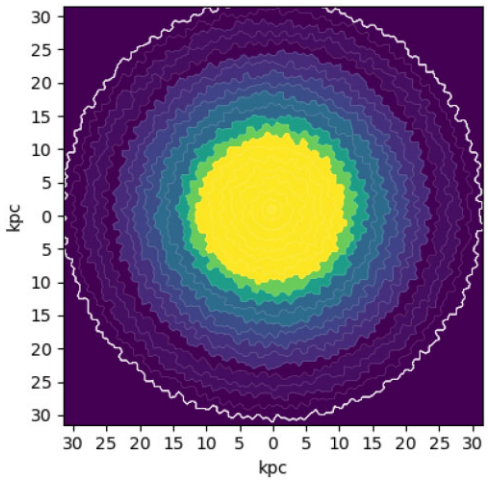

Figure 3. An illustration of the annular binned *F*150*LP* flux of J2318.

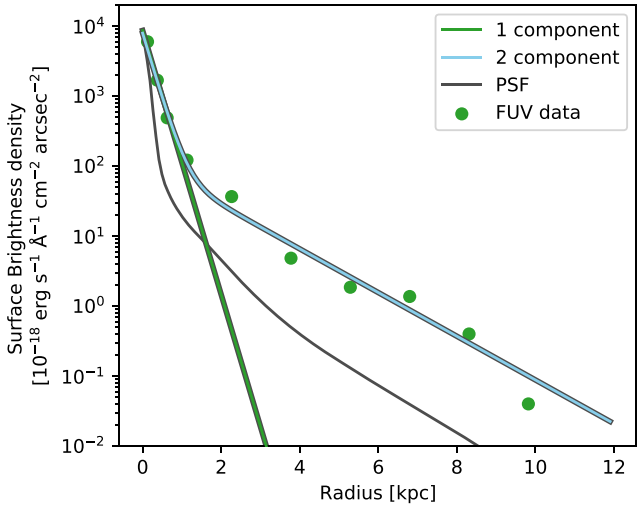

Figure 4. A comparison of the one-component UV model and the two-component model for J0004. This quite clearly shows the additional faint extended UV emission that is not captured by a one-component exponential fit. We also show the PSF of the *F*165*LP* filter, demonstrating that the extended emission is not due to the wings of the PSF.

the difference is that our spectral fitting aims to best estimate the behaviour of dust in the ultraviolet, whereas in the optical, the SMC and Milky Way laws are almost indistinguishable. The measured line fluxes are shown in Table 3 and derived quantities such as metallicity, ionization parameter, and dust extinction are shown in Table 4.

3.2.4 Characterizing the observed Lyα haloes

The most common way of characterizing low surface brightness Lyα-halo emission is to study azimuthally averaged radial profiles. However, when considering data that has been spatially binned, such as the Voronoi binning used here, doing photometry in simple circular annuli would lead to many cases, where the same Voronoi cell contributes to the flux in more than one annulus. The data and errors in adjacent annuli would therefore become correlated, which may be an issue for correctly fitting the surface brightness profiles.

To overcome this, we use a slightly different method that is based on Voronoi cells. Each Voronoi cell is assigned a distance to the centre of the galaxy that is computed as the mean of the distances to all the pixels that constitute the cell. We create a set of bins that are linear in radius, and then assign Voronoi cells to the bins based on whether their distance lies within the radial bin. This leads to almost circular bins with uneven edges, see Fig. 3, but ensures that a pixel is only counted once, even in radial averages. The error in each bin is calculated as the standard deviation of the fluxes of the included Voronoi cells.

When we construct the radial profiles, we also want to limit the maximum radius to which we fit in order to avoid numerical biases and detector edge effects. We therefore adaptively calculate a maximum radius to fit by stopping the radial profile, where two consecutive bins fall under a signal-to-noise of 0.75. We demanded two consecutive bins to ensure that any continuum absorption in Lyα did not stop our radial profile. From testing, we found that the exact choice of SNR threshold, if taken within reasonable limits (0.5 to 1.5), did not significantly impact the maximum radius selected by the method. The bin sizes are chosen to be small, 0.25 kpc, in the central part of the galaxies (central 1 kpc for all galaxies except J2318, where we used 3 kpc due to the complex extended morphology, see Section 4.2.5) and larger in the outskirts. The larger bin size was chosen for each galaxy to correspond to $\approx$10 px, which is slightly larger than the maximum size of a Voronoi cell. This makes sure that the annuli are complete and not broken up. We conducted several tests of binning pattern but found that the results were insensitive to them.

We then fit the Lyα as well as the FUV and Hα profiles constructed using the FUV brightest pixel as the centre. For FUV and Hα, we fit single exponential profiles. For Lyα, however, we want to characterize the level of contribution from an extended halo component and compare the results to high-redshift works. We therefore follow Leclercq et al. (2017) and construct the Lyα-model as the sum of two exponentials – one core component and one halo component – where the scale length of the core component is taken to be the same as the scale length of the FUV emission, but the amplitude is allowed to vary. The halo component is left unconstrained.

Additionally, to characterize the emission of Lyα properly, we need to address the fact that when using filter-based observations, such as our synthesized Lyα band, continuum absorption can become significant in FUV bright galaxy regions. Therefore we mask all Voronoi tesselations that show negative Lyα and that lie within 2 kpc of the brightest pixel during the fitting.

While this procedure allows us to directly compare results with Leclercq et al. (2017), we can also use the detail in our low-z data to explore other physically motivated models. Almost all our targets (with the possible exception of J2318, see Section 4.2.5) show apparent UV emission that is extended compared to the single exponential fit. We therefore extend the previous model by modelling the UV with a two-component exponential profile instead of a single profile.

Fig.4 shows the FUV profile of J0004 and clearly demonstrates this extended low SB component. The two-component profile, which is shown as the light blue line, follows the points at larger radii far better than the single component model. When comparing the sum of squared residuals outside 3 kpc, we find that the two component model reduces this by a factor of more than 2 on average.

Fitting the high and low SB points well at the same time is challenging, however, and we resolved this by fitting the UV data in two steps. First, we fit the central profile, as described above. This profile is used to generate a set of constraints for the full two-component fit. Specifically, the central component scale length is constrained to be the same as the one component fit, and the outer component scale length is constrained to be larger than that central

Table 5. Fluxes and luminosities in Lyα, Hα, and FUV.

Galaxy	Lyα flux [1]	Lyα luminosity[2]	Hα flux [1]	Hα luminosity[2]	FUV flux [3]	FUV luminosity[4]
J0004	560 ± 19	96 ± 3	970 ± 140	166 ± 24	29.6 ± 0.2	5.063 ± 0.036
J0139	42 ± 16	13 ± 5	298 ± 31	91 ± 9	9.7 ± 0.13	2.95 ± 0.04
J0156	1220 ± 51	276 ± 12	490 ± 158	111 ± 36	36.7 ± 0.5	8.29 ± 0.12
J0232	75 ± 10	23 ± 3	130 ± 55	41 ± 17	2.46 ± 0.08	0.762 ± 0.024
J2318	1433 ± 40	276 ± 8	2100 ± 130	405 ± 26	74.3 ± 0.43	14.30 ± 0.08
J2353	556 ± 15	90 ± 2.4	405 ± 60	66 ± 10	9.645 ± 0.169	1.567 ± 0.027
J2359	720 ± 30	150 ± 6	170 ± 100	35 ± 21	42.5 ± 0.3	8.88 ± 0.06

[1]Flux in units of 10^{-17} erg s^{-1} cm $^{-2}$. [2] Luminosity in units of 10^{40} erg s^{-1}. [3]Flux density in units of 10^{-17} erg s^{-1} cm $^{-2}$ Å^{-1}. [4]Luminosity density in units of 10^{40} erg s^{-1} Å^{-1}.

one. All other parameters are left free. In this model, we fit Lyα using three components: one core and one extended component, with scales and relative amplitudes set by the two-component FUV fit, and one halo exponential component.

In Fig. 4, we also show the PSF of the *F165LP* filter, noting that the second UV component is significantly brighter than the extended PSF wings even in J0004 which is one of the most compact sources. We also made an estimate of the potential contribution of nebular continuum to the UV emission based on the Hα surface brightness profile. The conversion factor between Hα emission and nebular continuum is approximately 0.003^{-1} at 1500 Å, and we find that the estimated nebular continuum is far below the measured UV surface brightness in all our targets. Any dust obscuration would reduce the nebular continuum contribution even further.

We can further leverage our low-z data by using our Hα observations and by considering the fact that, while the FUV should trace the stellar component that gives rise to the ionizing photons powering the Lyα emission, Hα should trace the gas, where the Lyα is produced. So we should really be comparing to Hα to determine whether Lyα is significantly extended and affected by spatial scattering. However, the signal-to-noise of the Hα data is lower than both the FUV and Lyα and the radius found by the adaptive radial profile (see description above) was quite small for Hα. Therefore, we were only able to use it to constrain the central part of Lyα. The approach we took was therefore to fit Lyα with two components, while constraining the centre using Hα instead of Lyα. The results of this are described in Section 5.4.

4 RESULTS

4.1 Global Lyα properties of the sample

First, we place our sample in the context of other Lyα-emitting galaxies and contrast global output with other studies. Global fluxes were measured in circular apertures designed to encapsulate the full Lyα halo flux, henceforth referred to as global apertures. We set the size of the global apertures by iteratively extending them from the UV brightest point and increasing their size by 10 pixels per iteration until the signal-noise-ratio in the next 10px wide annulus was below 1 i.e. it would add more noise than signal. The fluxes and luminosities of the Lyα, Hα, and FUV measured in this aperture are listed in Table 5, while derived dust extinction, metallicity, and O32 $\equiv$ [O III]5007/[O II]372,729 ratio are shown in Table 4. Errors on the Lyα, Hα, and FUV fluxes were derived as the standard deviation of the measurements made in each layer of the MC cube (see Section 3.2.2).

We robustly detect Lyα ($>5\sigma$) in the global aperture in six out of seven targets. In the remaining target, the global aperture shows a $\sim 3\sigma$ detection. We stress that this is in a large aperture and therefore is heavily impacted by central absorption. We detect Lyα emission around all galaxies when considering binned annuli. The escape fractions and equivalent widths of Lyα are presented in Table 6. The Lyα escape fraction is defined as

$$f_{\rm esc} = \frac{\rm Ly\,\alpha}{8.7 \times \rm H\,\alpha}, \tag{5}$$

where Hα is corrected for dust extinction and 8.7 is the assumed intrinsic Lyα to Hα ratio. We find that our sample spans a large range in escape fractions, from 0.7 to 37 per cent. The equivalent widths ranges from 4.4 Å in J0139 to 57 Å in J2353.

Table 6. Table of escape fractions, equivalent widths of Lyα, measured halo fractions from the three component model and the size of the global aperture used.

Galaxy	Lyα $f_{\rm esc}$	Lyα EW [Å]	HF	Aperture [arcsec]
J0004	0.048 ± 0.007	15.3 ± 0.4	0.68 ± 0.02	3.6
J0139	0.007 ± 0.003	3.3 ± 0.9	0.30 ± 0.30	1.2
J0156	0.23 ± 0.08	26.2 ± 0.9	0.78 ± 0.01	4.0
J0232	0.05 ± 0.02	23.3 ± 2.5	0.58 ± 0.09	1.2
J2318	0.052 ± 0.004	15.4 ± 0.4	0.90 ± 0.17	4.8
J2353	0.15 ± 0.02	46.7 ± 1.2	0.81 ± 0.08	1.6
J2359	0.370 ± 0.22	13.4 ± 0.4	0.48 ± 0.05	2.8

In Fig. 5, we show the correlations of the Lyα escape fraction and EW with some nebular properties of the gas. Specifically, we show correlations with dust extinction ($E(B-V)$), ionization parameter traced by the O32 ratio, and the metallicity of the galaxies measured from the O3N2 index using the Marino et al. (2013) calibration. In addition to the seven galaxies presented in this work, we also show data for the LARS sample from Melinder et al. (2023, redshift range $0.028 \leq z \leq 0.181$) and a large collection of low redshift ($0.02 \leq z \leq 0.44$) COS observations taken from the Lyman Alpha Spectral Database (LASD; Runnholm, Gronke & Hayes 2021; Hayes et al. 2023, and references therein). The optical data for all galaxies comes from the SDSS. We note that these different samples have very different selection effects and observational methods and would not necessarily be comparable; we show this comparison primarily to illustrate that our sample does not appear different from any of the others, regardless of how the measurements were made. We see substantial scatter in all of the displayed relations, but when taken in conjunction with large archival samples, some clear trends do emerge. In fact, as indicated by the Kendall-tau correlation metrics displayed in the panels, all of the correlations become statistically significant with some correlations, such as Lyα EW and O32 ratio and the anticorrelation between Lyα $f_{\rm esc}$ with

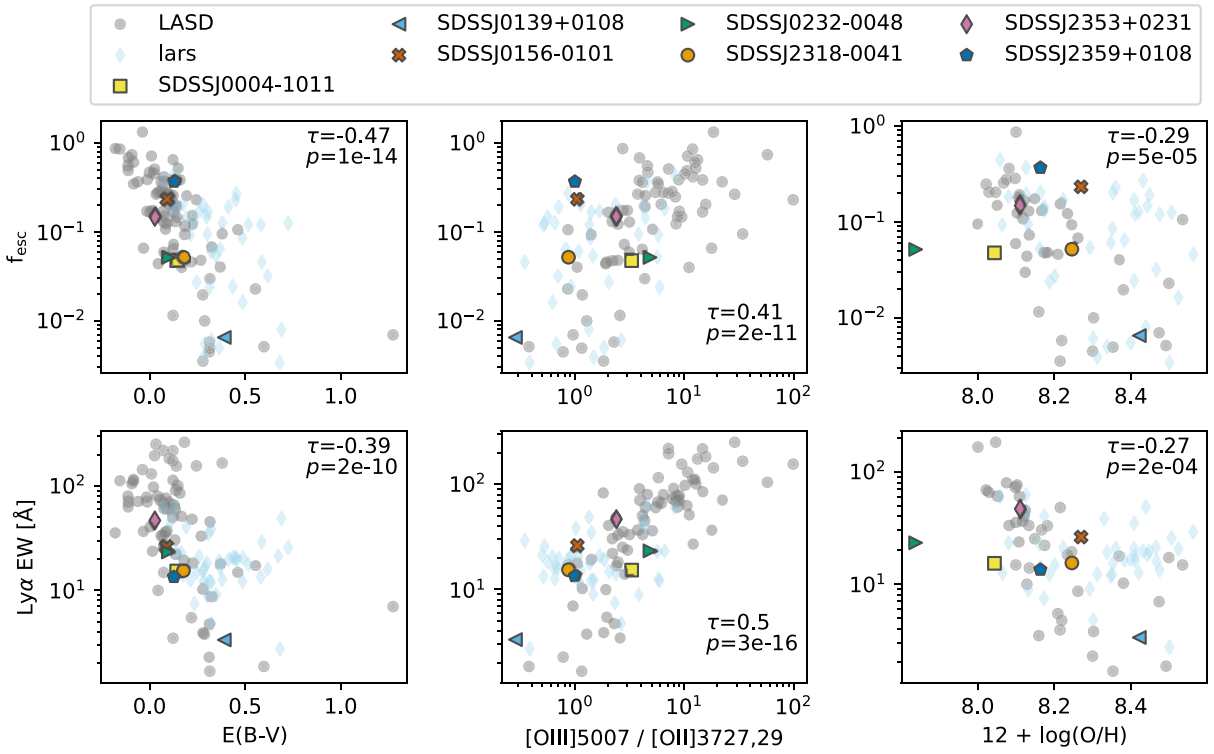

Figure 5. Correlation plots of the global Lyα properties of our sample. Grey points indicate galaxies with Lyα measured in COS spectroscopy using the LASD data base (Runnholm et al. 2021). Light blue diamonds show the distribution of Lyα properties of the LARS and eLARS galaxies measured in a global aperture. The τ in each panel indicates the Kendall-tau correlation coefficient of all galaxies shown, and p indicates the corresponding p-value.

dust extinction ($E(B-V)$) having p-values as low as 10^{-16} and $\tau \approx 0.5$.

4.2 Detailed discussion of the sample

In this section, we discuss our observations and our sample of galaxies in more detail since some of our objects show interesting features in all observed bandpasses, and careful consideration of the surface brightness profiles and fits are useful for interpreting subsequent results.

For each target, we present one figure akin to Fig. 6. Panel **a** shows a three-colour image of Hα in red, FUV in green, and Lyα in blue with arcsinh scaling. The rest of the top row (panels **b**–**d**) shows the individual bands with the same colour assignment but log scaled. The second row (panels **e**–**g**) shows binned radial profiles and multiple component fits to the data (two components for UV and Hα and three components for Lyα).

4.2.1 J0004

J0004 is shown in Fig. 6 and has a notably compact and circular appearance even in high spatial resolution *HST* imaging. The total escape fraction of Lyα is quite low at 5 per cent, due to strong continuum absorption in the centre of the galaxy. The UV shows a sharp peak with a scale length of 0.23 kpc and then a clear, flatter outer component (scale length 1.39 kpc), which is much fainter (the amplitude difference is approximately a factor of 100). Despite taking the extended UV emission into account, we find that there is still evidence for extended halo emission in the Lyα-profile with the extended outer component showing a distinctly higher amplitude relative to the centre than in the FUV as well as a slightly flatter slope (scale length of 1.65 kpc). There are also hints that the Lyα is flattening out even further at radii above 10 kpc; however, the remaining data are too low signal-to-noise to determine this with any certainty. The measured Lyα halo fraction of this galaxy is 0.69 ± 0.03.

Turning to the Hα surface brightness profile, we note firstly that it is only well traced out to a radius of ∼4 kpc. The data seem well described by two exponential profiles. The slope of the Hα is distinctly shallower than the core component of the UV. This could indicate that ionizing photons produced in the most UV bright regions travel some distance before being absorbed and ionizing the gas. We will discuss this further in Section 5.4.

4.2.2 J0139

The morphology of J0139 is dominated by two star-forming clumps, which can also be seen as two distinct bumps in the radial profile. Despite the clumped morphology, the FUV radial profile is reasonably well described by a central exponential decline, and there is compelling evidence for extended FUV emission (panel **e** of Fig. 7) that is well captured by a two-component FUV model. The galaxy shows strong central absorption but has weak Lyα emission around the clumps. Panel **g** demonstrates that the Lyα is very weak in this target and that constraining the contribution from a Lyα halo in this case is difficult. This is reflected in the uncertainty on the measured halo fraction 0.19 ± 0.28, which is consistent with zero halo contribution, as we would expect from looking at the few Lyα data points.

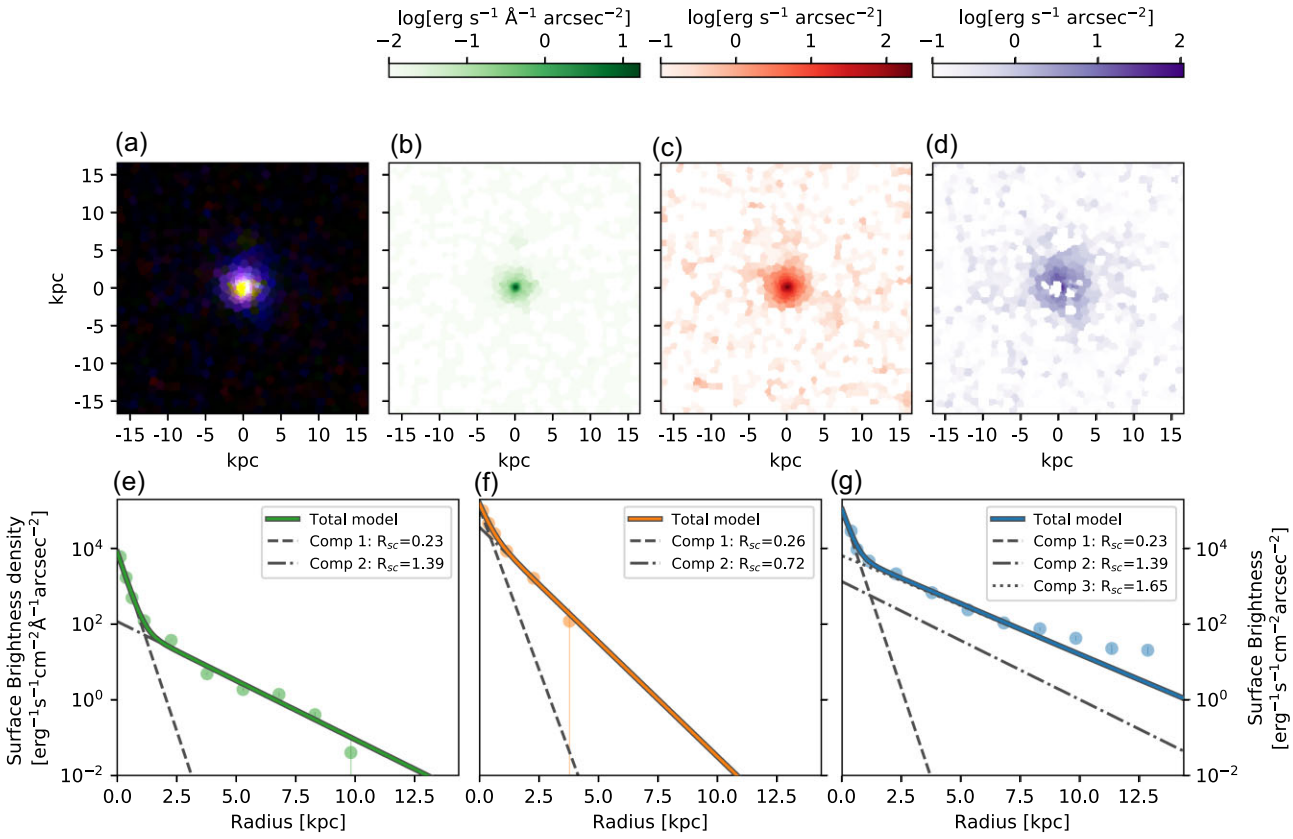

Figure 6. Images and surface brightness profiles for J0004. All surface brightnesses are given in units of 10^{-18} erg^{-1} s^{-1} Å^{-1} arcsec^{-2}: **a)** Lyα, FUV, and Hα composite image with arcsinh scaling to highlight low surface brightness. **b)** Log-scaled *F165LP* UV image; **c)** Log-scaled Hα image; **d)** Log-scaled Lyα image; **e)** binned radial surface brightness profile of the FUV, together with the best-fit two-component model of the emission. Note that the FUV emission is given in flux densities rather than fluxes, i.e. [erg s^{-1} Å^{-1} cm^{-2} arcsec^{-2}] since it is continuum emission rather than integrated line emission; **f)** binned radial surface brightness profile of the Hα, together with the best fit two component model of the emission; **g)** binned radial surface brightness profile of the Lyα, together with the best fit three component model of the emission.

The Hα emission is quite weak outside the very central parts of the galaxy, and the pronounced two-clump morphology of the system drives the fit to find a flat second component. One could consider several ways of treating this morphology, including removing the data point at 3 kpc, which would return the profile to an approximate exponential decline, or modelling this extra component using an additional core component modelled in two dimensions. However, doing detailed 2D modelling of our targets is beyond the scope of this work. We will, however, further examine the Hα properties of these galaxies in a forthcoming paper using deep ground-based observations.

4.2.3 J0156

J0156 (Fig. 8) is morphologically similar to J0004 i.e. circular and compact. However, as is clear from the three colour image there is also evidence for a secondary structure to the north-east of the main galaxy, which could be a fainter star forming knot or a remnant of an interaction that possibly caused the central starburst. The Lyα emission from J0156 is significantly stronger than J0004 (with a total luminosity of 1.2×10^{42} erg s^{-1}), and it has a global escape fraction of 23 per cent. One possible reason for this is lower central continuum absorption. While we cannot measure the level of continuum absorption with our data we note that this galaxy shows fewer absorption dominated pixels, i.e. pixels that are negative in the Lyα image, in the UV bright regions than the other targets and the implied escape fraction for the central 1 kpc is around 15 per cent.

Examining the surface brightness profiles, beginning with the FUV in panel **e**, we note several similarities with J0004, specifically a steep, bright central core component and a flat outer component. We do note, however, that in this case, there are a significant number of UV points that show an even flatter slope outside of 20 kpc before the signal-to-noise drops below our threshold. Similar extended emission is also seen in the Lyα SB profile, but the Lyα halo component is flatter and significantly brighter relative to the core brightness than its FUV counterpart, leading to a large measured halo fraction of 0.78 ± 0.012.

4.2.4 J0232

J0232 (Fig. 9) is the smallest galaxy in our sample in both angular and physical size. The FUV profile shows very compact emission and some hints of turnover at a radius of 5 kpc. The Hα shows similar behaviour but unfortunately cannot be traced out to this radius, leaving us unable to confirm the presence of a similar turnover. The Lyα profile has an inner core that is well-described by the FUV and Hα radial profile fits, but has a distinct and very extended secondary emission component that is significantly flatter than the

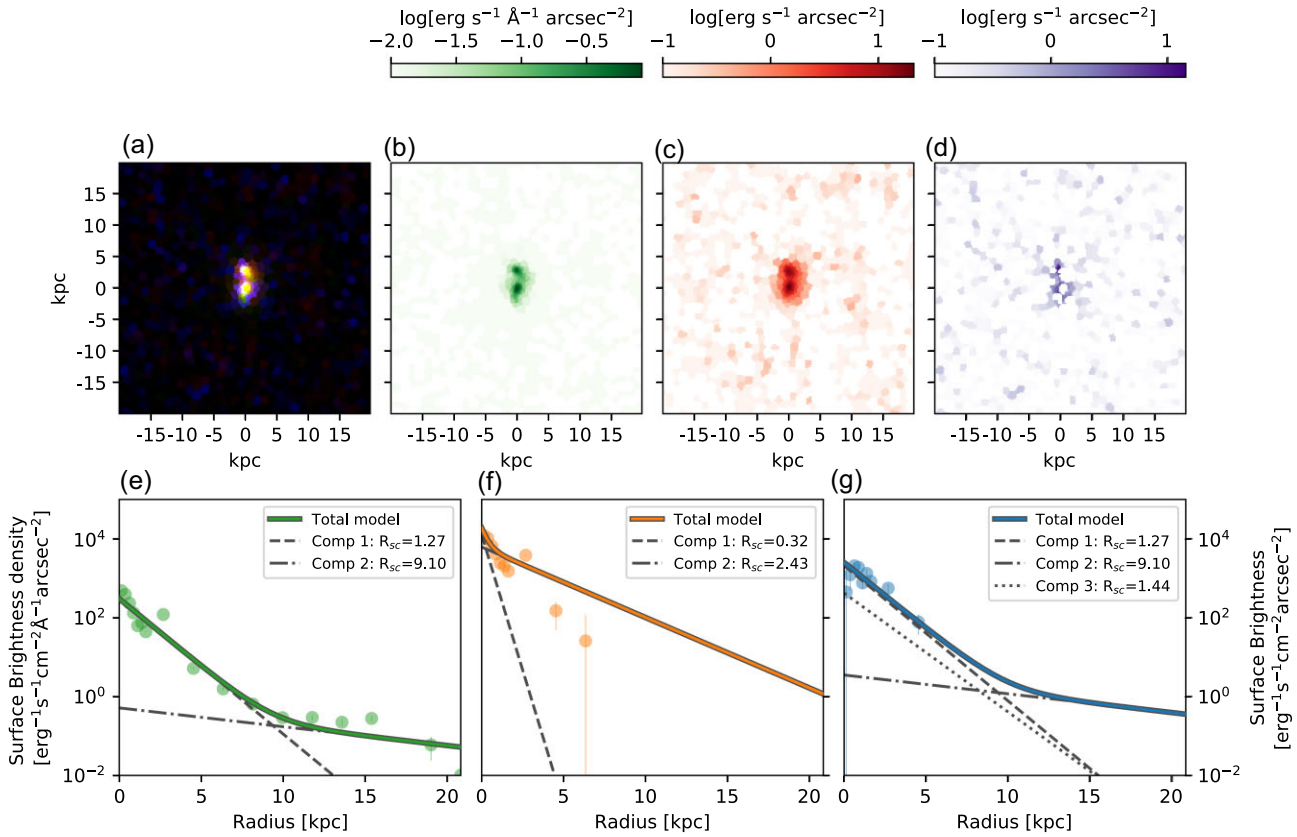

Figure 7. Lyα, Hα, and FUV profiles for J0139. For a detailed description of each panel see Fig. 6.

FUV secondary component. However, the strength of this extended emission relative to the core is lower than in J0004 and J0156, leading to a halo fraction of 0.58 ± 0.09.

4.2.5 J2318

J2318 is the largest and structurally most complicated of the galaxies in our sample. The main structure of the galaxy in the FUV is composed of a number of star-forming clumps, many of which also emit bright Hα. There are also additional structures visible both in FUV and Hα, including a series of emission spots tracing a faint arm-like feature to the north-east, and a strong clump of Hα emission to the north-west.

Attending now to the radial profile of the FUV in panel **d**, we see that it is quite uneven and 'bumpy', reflecting the clumpy structure of the galaxy. However, unlike the profiles of the other targets, it follows a relatively straight exponential decline, as opposed to a bright central emission core and a faint extended component. The FUV points do show a slight flattening at the very highest radii, around 20 kpc, but the SNR of the data is insufficient to trace this further. This smooth decline in surface brightness leads to issues with our model description. The data itself strongly resembles a single exponential, and this is corroborated by the fit returning similar scale lengths for both components but one having a smaller amplitude. Our conclusion, in this case, is that a single exponential decline is the best description of the surface brightness profile while stopping short of spatially decomposing the galaxy and simultaneously fitting each individual clump.

Turning now to the Hα and Lyα profiles, we note that they are very similar to the UV, both following smooth exponential declines. However, we do note that the scale length of the Hα profile is slightly larger than that of the FUV, and that the Lyα scale length is in turn slightly larger than that of Hα. Together, this indicates that ionizing photons travel some distance before ionizing hydrogen atoms, creating Hα and Lyα photons and potentially that Lyα photons then scatter even further from the site of creation. One should again keep in mind that we cannot trace Hα as far as Lyα and that the slope of the Lyα may be impacted by those large radius points. The fact that a single exponential dominates the fit leads to a large halo fraction of 0.90 ± 0.17.

4.2.6 J2353

While the overall morphology of J2353 is similar to J0004 and J0156, panel **a** of Figs 11 and 1 show that it is more extended along one axis. Contrasting panels **a** and **c**, we also note that the Lyα appears significantly more circular than the FUV. Similar contrasts between UV and Lyα have been observed in edge on systems, such as Mrk 1486 (Duval et al. 2016; Rasekh et al. 2021), and may be due to preferential Lyα escape in the direction of galactic outflows emanating from the plane of the galaxy.

Attending next to the surface brightness profiles, we see that the FUV has a very distinct core with a scale length of 0.4 kpc and a secondary faint component with a scale length of ≈3.2 kpc. There are also hints at a further, even flatter component at very large radii. We are unable to trace the Hα profile very far but see that it is well

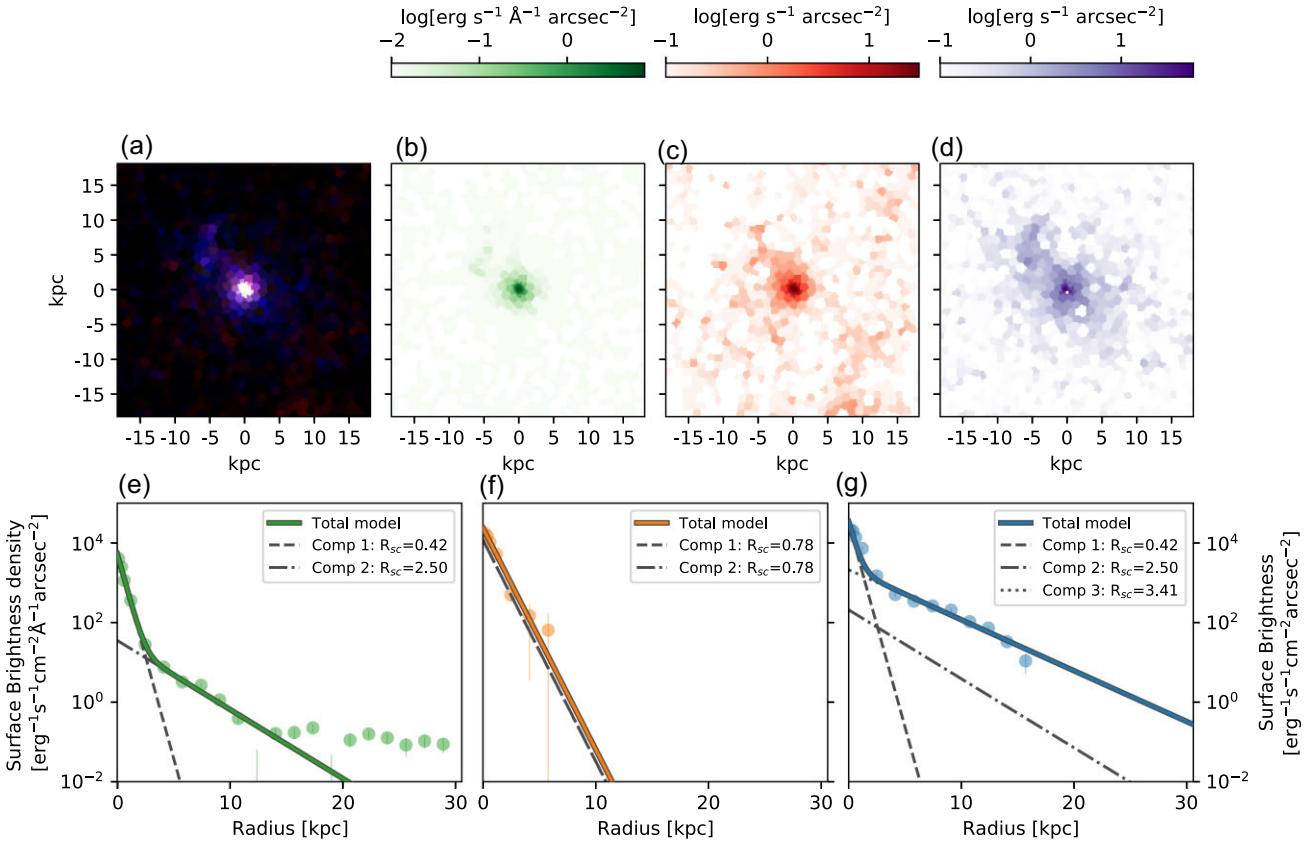

Figure 8. Lyα, Hα, and FUV profiles for J0156. For a detailed description of each panel see Fig. 6.

parametrized with two components, with a sharp central peak and then a flatter decline, but the number of data points is low and the profile can be adequately described with a single profile with a scale length around 0.7 kpc, i.e. larger than the core scale length of the UV.

The Lyα shows some interesting behaviour, with a distinctly flatter decline than the FUV profile, almost directly from the centre. This, taken in conjunction with the Hα may indicate that ionizing photons are travelling some distance from the centre before ionizing. The data has insufficient signal to noise to trace the Lyα far enough to tell whether the secondary FUV emission also manifests in the Lyα. However, the non-detection of Lyα at large radii may indicate that the secondary FUV component is coming from a stellar population that does not produce significant ionizing radiation, and hence, no Lyα. This situation does not match a classical extended halo. However, if we interpret the core FUV as the primary ionizing component, the Lyα extension essentially describes a halo around this component. We will refer to this as an inner excess to differentiate it from a more classical halo. The fraction of emission from this inner excess is quite large: 0.81 $\pm$ 0.08.

4.2.7 J2359

J2359 is perhaps one of the most interesting objects in our sample. In the optical image (last panel of Fig. 1) the galaxy does not appear particularly different from the rest of the sample, with a compact morphology closely resembling that of J0232 and J2353. However, when we look at the line map in panel **c** of Fig. 12, the Hα emission from J2359 is very diffuse and in fact appears distinctly less bright in the central regions of the galaxy, contrary to all the other galaxies studied here. The Lyα to Hα ratio in the central 0.5 kpc radius is 12.6 $\pm$ 2.9 – a 1.3 sigma deviation above the expected recombination ratio of 8.7.

We interpret this as a sign of the removal of gas from the interior of the galaxy by feedback from the formation of the central star clusters. A similar situation is seen in the local starburst galaxy ESO338-IG04, where the region around one of the clusters presents a 'hole' when viewed in both Hα and [O III] (Hayes et al. 2005; Östlin et al. 2009; Bik et al. 2015). Additionally, this evacuated region is exceptionally bright in Lyα (Hayes et al. 2005) – a situation that is very much akin to J2359. The key difference between these cases is that for J2359 the vacated region is $\approx$10 times larger than in ESO338-IG04, and while the galaxy is also quite small, this probably points to an episode of exceptionally strong feedback.

We also note that the observed $E(B-V)$ of 0.13 (see Table 4) would imply an escape fraction of $\approx$30 per cent for Lyα, even without considering any additional effects from resonant scattering. The central escape fraction of 140 $\pm$ 30 per cent is clearly exceptional, at least from the central regions of a galaxy. This naturally raises the question of how such a bright Lyα may be created without Hα emission showing from the same region. There are essentially three possibilities. First, it may be the result of scattered Lyα radiation from an outer emission region, i.e. Lyα that is actually produced approximately cospatially with Hα but that then scatters back towards the centre of the galaxy. Essentially, this scenario implies that what we are seeing as a ring in Hα is actually the limb brightening of a spherical shell emitting gas. Resonant scattering of Lyα emitted from

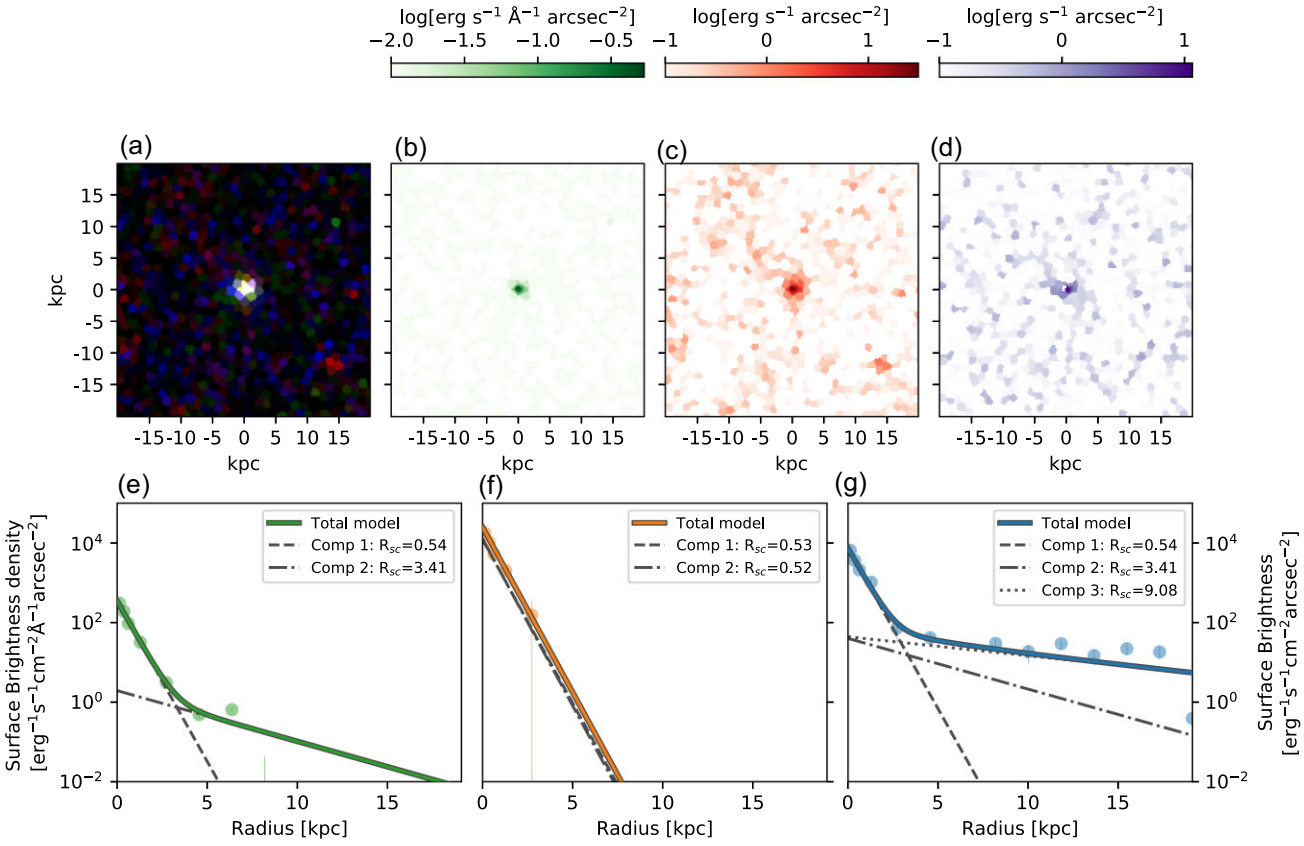

Figure 9. Lyα, Hα, and FUV profiles for J0232. For a detailed description of each panel see Fig. 6.

such a shell would act as a smoothing of the structure and elevate the Lyα to Hα ratio in the centre.

Second, it may be due to collisional excitation of the Lyα line. In principle, this mechanism can create Lyα emission with a much higher Lyα to Hα ratio than recombination. However, the production efficiency of collisional Lyα depends on the square of the gas density. The implication of relatively low densities in the centre of the galaxy from the Hα observation would then suggest that this is not a dominant mechanism.

The third is scattering in a dusty and clumpy medium. This mechanism was initially proposed by Neufeld (1991) as a situation that would boost Lyα EW. In this case, the resonant Lyα line will scatter on the surface of the clumps and will naturally escape through low-density channels, while non-resonant emission will be captured and absorbed by the dense clumps. However, this scenario requires very specific gas and dust conditions to work – specifically requiring the medium to be very static relative to the Lyα radiation, since a velocity offset between the clumps and the Lyα photons would allow them to penetrate into the dense dusty clumps and be efficiently extincted (for details, see Laursen, Duval & Östlin 2013).

The general behaviour of the Lyα radial profile is very similar to J2318, showing a inner excess rather than a classical halo. Nevertheless the emission from the extended Lyα component is quite strong and the halo fraction of this target is 0.48 ± 0.05.

4.3 Lyα halo sizes

In this section, we discuss the comparison between our targets and high redshift observations. We will primarily consider the results from the two component model here, as that is most directly comparable to the work of Leclercq et al. (2017), in particular when comparing UV and Lyα scale lengths. It is worth noting that the comparison of halo fractions would be largely unaffected by using the three-component model, as demonstrated by Fig. 13, which shows the halo fractions of the two-component model versus the halo fractions of the three-component model. We find that the new model with two FUV components can describe the full FUV profile significantly better, but that the extended UV is very faint compared to the peak core flux. In particular, the relative core to halo flux level in the UV is much higher than in the Lyα, which means that the additional UV component has only marginal effects on the Lyα halo fit. The result is that the halo fractions that we measure are largely unchanged, with decreases on the order of a few per cent, as shown in Fig. 13.

Panel **a** of Fig. 14 shows the scale length of the Lyα halo component versus the scale length of the UV emission. The grey points from Leclercq et al. (2017) are scattered around the 10:1 line, and the majority of our galaxies fall within this distribution. However, our galaxies tend to lie towards smaller Lyα over FUV scale length ratios, with the smallest ratios being those of J2318 and J0139. One should keep in mind that J0139 has a very weak Lyα detection, and thus no extended Lyα halo is present in our data, and that J2318 has a very complex morphology, which leads to a single exponential decline in the light profile rather than a clear core and halo as seen in other targets. To establish whether our seven targets are consistent with the high-z distribution, we performed a two sample KS test on the Lyα halo to FUV scale length ratios. We found that our sample has a statistically significantly smaller ratio (mean ratio 5.6 versus 12 kpc in Leclercq et al. (2017)), with a p-value of 0.01. When J0139 and J2318 are excluded, the mean is 7.4 kpc and the statistical

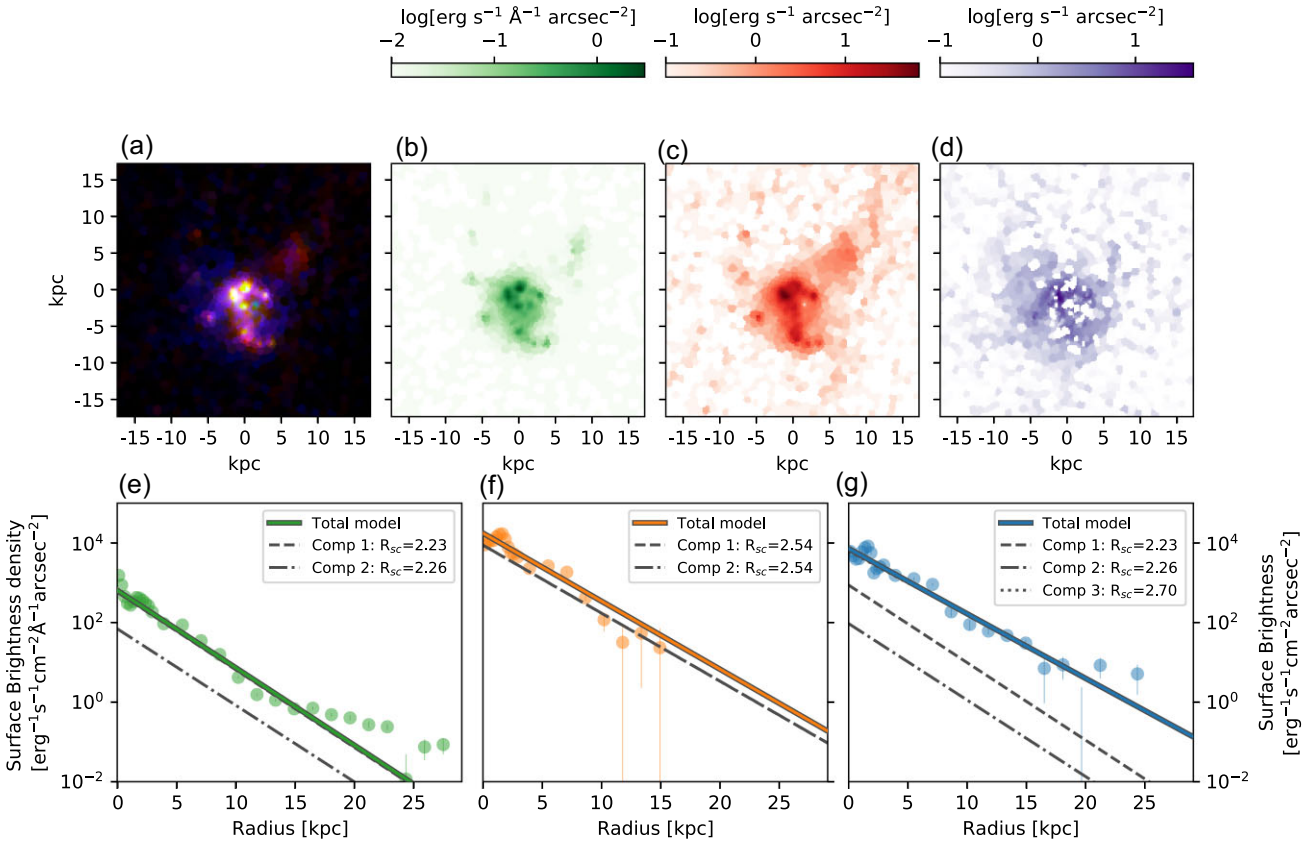

Figure 10. Lyα, Hα, and FUV profiles for J2318. For a detailed description of each panel see Fig. 6.

significance drops to 0.26, i.e. the distributions are not significantly different, although it should be noted that the number of data points is in this case very low.

We note that the LARS points have a greater overlap with high-redshift points in the FUV to Lyα ratio, but also that they extend to smaller sizes both in FUV and Lyα. This is most likely not due to LARS galaxies being smaller than galaxies observed by Leclercq et al. (2017), but rather that the observations are resolving internal structures (star-forming clumps) in these low-z galaxies. At the most compact end, we are observing scale lengths as small as 0.2 kpc, which would correspond to 0.02 arcsec, or about half a *HST* pixel at $z = 3$, which would not be observable. Nevertheless, if we include the LARS points in the size-ratio analysis, the difference between the low and high redshift distributions is no longer significant (p-value of 0.14).

Panel **b** of Fig. 14 shows the Lyα halo luminosity as measured from the fitted model against the halo fraction (HF) of Lyα. We define the halo fraction as the fraction of model flux coming from the halo component compared to the total model flux when both are integrated to infinity. It is clear that the distribution of our galaxies is quite consistent with the high-redshift results, which we confirm using a two sample KS test (p-value = 0.6). Our seven targets mostly scatter between 50 and 85 per cent contribution from the halo with one target having a lower HF of 0.25 but with very significant measurement uncertainties. This panel also shows the distribution of points from the LARS sample, and when those are included, we see that the relative halo contributions at low redshifts appear to be higher than at high redshifts, although it should be noted that this is largely driven by points that lie at Lyα luminosities below what is observed in the Lyα selected sample of Leclercq et al. (2017).

5 DISCUSSION

5.1 Improving the UV modelling

The comparison with Leclercq et al. (2017) used a fitting methodology that was as similar as possible to the procedure employed in that paper. However, at low-z cosmological surface brightness dimming is significantly less than at the redshifts probed by Leclercq et al. (2017, a factor of >200 less when compared to redshift 4), which allows us to probe lower SB FUV emission. As can be seen from Figs 6–12 and Fig. 4, the UV light profile is not exponential beyond radii of a few kpc, but is centrally peaked within this radius and then flattens (Section 5.1). Similar results have already been noted by Izotov et al. (2016) and are likely attributable to a population of older stars that formed recently enough to remain bright in the UV but were not formed in the current burst of star formation. Even if clumpy and sparsely distributed, the light profile of such a population may appear to decline roughly exponentially when azimuthally averaged, as done here.

This faint, additional component would not be visible in the $z >$ 3 studies because cosmological surface brightness dimming would place it below the detection thresholds (see Section 5.2). These known high-z galaxies also subtend small angular sizes, and one cannot bin over very large areas to collect diffuse light. Stacking of *HST* data remains a possibility to determine whether similar UV light profiles are in place at high z, but this is beyond the scope of this work. If the *HST* cameras cannot detect the extended continuum light but the Lyα is captured by the much higher surface brightness sensitivity of MUSE, then halo fractions could be artificially overestimated in high-z samples that combine the two data sets and a parametric approach.

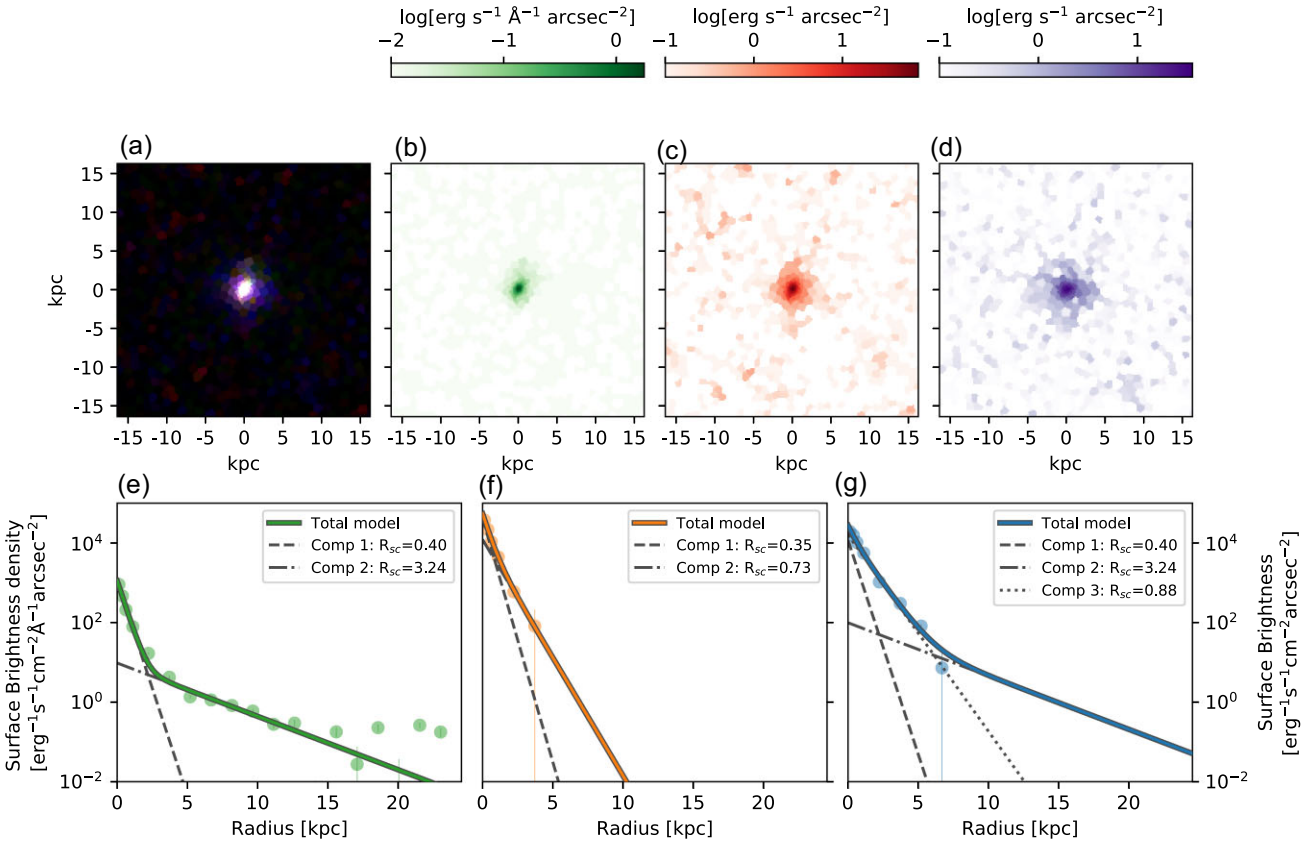

Figure 11. Lyα, Hα, and FUV profiles for J2353. For a detailed description of each panel see Fig. 6.

If we want to study extended Lyα haloes and specifically the Lyα emission that is not associated with stellar UV emission, it could be important to take this faint stellar component into account. However, as we discussed in Section 4.3, this additional UV emission seems to have very little effect on the Lyα profile fit, and therefore despite the addition of a faint UV component, there is still evidence for significant extended Lyα. In two cases, however, we note that the Lyα profile is best described with an 'inner excess' component that has an intermediate scale length, i.e. larger than the core UV component but smaller than the faint outer UV component. We interpret this as evidence that only the central bright UV component is the primary source of ionizing photons, leading to the production of extended Lyα emission either through escape of ionizing photons – producing Lyα in situ – or resonant scattering.

Further support for this picture comes from the age maps produced by the SED fitting routine. We measured the UV luminosity-weighted age of the region of the galaxy dominated by the inner component and contrasted it with the age measured in an annulus around that. We find that for both targets that show an inner excess, the central age is around 3 to 4 Myr and the outer age is 600 to 700 Myr, which implies that the core is producing ionizing photons at essentially maximum efficiency, whereas the outer component is comparatively not producing any ionizing photons (Leitherer et al. 1999). The presence of an old population may bring into question the analogue nature of these targets to high-z observations, but we note that the observed ages are nevertheless significantly lower than the age of the universe at the redshifts of the high-z comparison samples ($z \sim 4$) and thus that such populations may exist but would be very hard to observe (see also Section 2.1).

5.2 Comparison with high-z samples: selection methods and methodology

This project was designed to image Lyα haloes in a way that allows their extended light to be quantitatively contrasted with the data from high-z studies. The objective, however, is limited by both technology and selection effects. No FUV IFUs exist in space and we must instead use narrow-band imaging. Moreover, no current satellite has a large-volume Lyα survey capabilities, so all targets must be pre-selected with unknown Lyα properties, before observation with *HST*.

Our galaxies were selected based on star formation and UV properties, specifically chosen to sample highly star forming galaxies even compared to the main sequence at $z \gtrsim 3$, but this differs substantially from typical LBG and LAE selections. MUSE samples are a combination of UV preselection from *HST* imaging for sources brighter than 27th magnitude in the *F775W* filter and emission line selection for sources fainter than this in the *HST*. However, since only galaxies with significant UV continuum detections can have their sizes measured, it is likely that faint, high-EW galaxies at high-z will enter the comparison samples. This will lessen the impact of emission line selection effects. As mentioned in Section 2.1, our UV absolute magnitudes were selected to overlap with the fainter quartile of those in Leclercq et al. (2017), and extend to reach the magnitudes of the $L^\star$ LBGs of Steidel et al. (2011). We also show (e.g. in Fig. 14) that the UV scale lengths of our sample closely agree with those found for LAEs and LBGs at $z > 3$, and therefore argue that differences resulting from selection should be relatively minor. We still caution, however, that these differences cannot be quantified and that there is no way to test these effects with current technology.

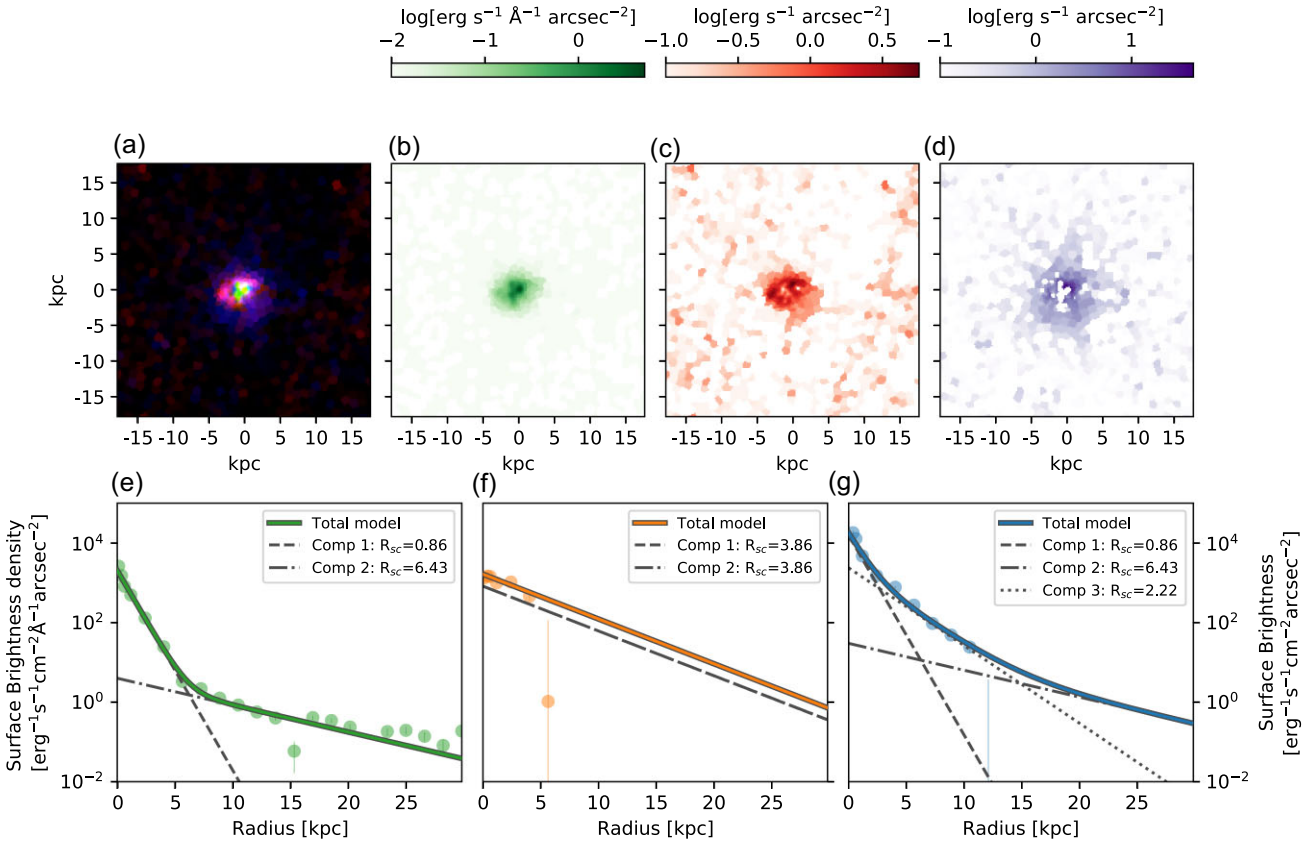

Figure 12. Lyα, Hα, and FUV profiles for J2359. For a detailed description of each panel see figure 6.

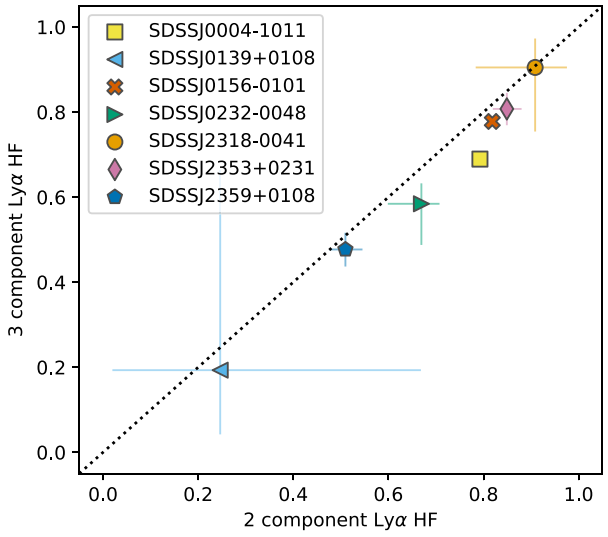

Figure 13. Comparison of the Lyα halo fractions derived using a three component Lyα model (y-axis) to a two component Lyα model (x-axis).

We further consider the relative depths of our Lyα observations compared to Leclercq et al. (2017), by examining the signal-to-noise ratio in the binned radial profiles as a function of surface brightness. We reach a SNR of three roughly at an average surface brightness of $\sim 3 \times 10^{-17}$ erg s^{-1} cm^{-2} arcsec^{-2} (e.g. panel **g** in Figs 6 to 12). In order to compare this to the results of Leclercq et al. (2017), we need to take cosmological surface brightness dimming into account. For this simple comparison, we assume a single redshift of 0.25 for our galaxies and four for the MUSE surveys, implying a difference of a factor of 256 in surface brightness. If the faintest isophotes that we can detect at $z \approx 0.25$ were instead produced by galaxies at $z = 4$, the corresponding surface brightness would be $\simeq 1 \times 10^{-19}$ erg s^{-1} cm^{-2} arcsec^{-2} – this is indeed very similar to the detection limits given for individual galaxies in the MUSE-Deep sample (Leclercq et al. 2017), and also corresponds to the faintest level shown in the full stack of LBGs by Steidel et al. (2011). We conclude that our observations reach comparable depths in the restframe to those measured at high-redshifts.

5.3 Do characteristic Lyα halo sizes evolve with redshift?

Despite the differences in selection, observation techniques and potential variation in observation depth our results are broadly consistent with published results from high redshifts. Panel **a** of Fig. 14 shows that our galaxies appear to exhibit slightly smaller Lyα to FUV scale length ratios compared to high redshift.

While the small number of our targets limits the strength of this conclusion, the effect is strong enough that it warrants a discussion of what physical differences in the CGM of these galaxies could cause a drop in the observed Lyα to FUV scale length ratio. If the neutral gas in the CGM is clumpy instead of homogeneous, Lyα photons could escape out through the lower density channels between the clumps, requiring less spectral redistribution for an optically thin path out of the galaxy to appear. Since scattering is essentially a random walk process, this would reduce the path length Lyα photons travel before escape, lowering the scale length of the halo.

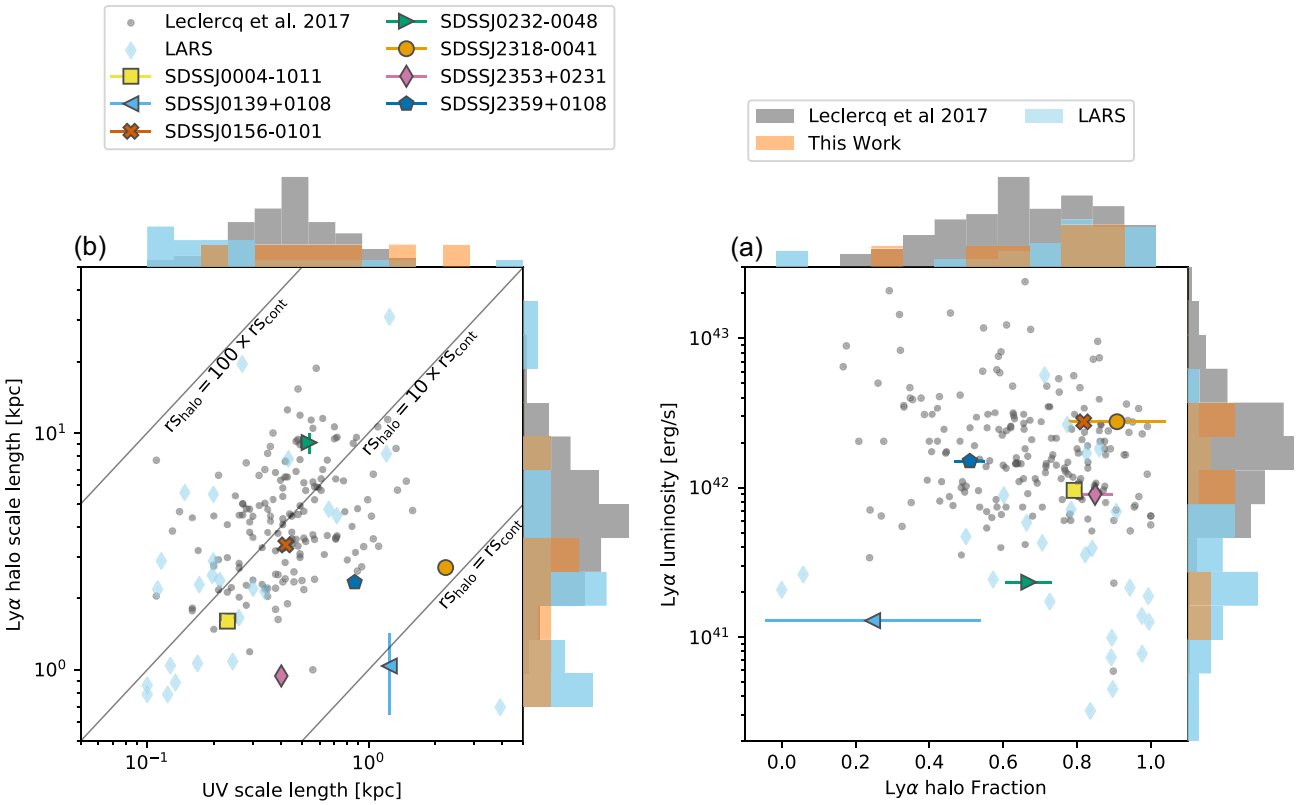

Figure 14. Panel **a**: Relation between halo scale length and UV scale length. Grey points indicate galaxies from Leclercq et al. (2017). Light blue points are measurements from the LARS sample (Rasekh et al. 2021). Diagonal lines denote lines of constant relation between the Lyα halo and FUV scale lengths, denoted $rs_{\rm halo}$, and $rs_{\rm cont}$, respectively. Panel **b**: Distribution of measured halo fractions versus the Lyα luminosity of the galaxy. Histograms show the distributions of the points for the three samples (MUSE, LARS, and this work).

Similar effects might be achieved if the velocity structure in the CGM has significantly changed between low and high redshift. Spatially resolved spectroscopic observations of the Lyα emission from the halo may be able to provide some clues, however, such observations are very challenging at low redshift. Both of these scenarios assume that the production of the Lyα halo is dominated by scattering.

Another potential cause of reduction in relative Lyα to FUV size could come from dust being present in the haloes of lower redshift galaxies. It is possible that lower-z systems have had more time to produce dust and, in particular, transport this dust from the central star-forming regions to the outskirts through outflows. This could be observable with sensitive ground-based observations of Hα and Hβ, and we will examine this in a forthcoming work.

However, due to the sample size, the statistical effect is not very strong, and including the results of the LARS galaxies reduces the statistical significance to the point where we cannot conclude that there is a difference between the distributions.

Turning to panel **b** of Fig. 14, we note that the halo flux fraction distribution of our seven galaxies is statistically consistent with the high-z sample with a mean around 70 per cent. In this case, adding the LARS points would indicate that halo fractions at low-z are larger than at high-z, however, we note that this effect is driven mostly by low Lyα-luminosity galaxies that would not be observed at high-z. These galaxies have very little central Lyα-emission – leading to very high observed halo fractions.

When taken together, these observations seem to indicate a potential reduction in the relative extent of Lyα compared to the FUV, but when all low-redshift observations are taken into account, this effect is not seen, and the results are inconclusive. This brings us to the conclusion that despite the elapse of ∼10 Gyr between the low- and high-redshift samples, there is not much change in the spatial distribution of Lyα. This conclusion holds most strongly in absolute terms (measures of the physical sizes) but also in relative terms (with respect to the ultraviolet continuum) when considering all low-z galaxies together. The fact that we appear to be sampling similar objects and haloes to similar depths provides additional confidence in this lack of evolution. We further consider the spectroscopic results of Hayes et al. (2021), in which we identified no evolution in the kinematic properties of Lyα between comparable low- and high-z galaxy samples (again using *HST*/COS and VLT/MUSE, respectively). Taken as a whole, these results are encouraging for the use of low-redshift observations in efforts to probe the processes ongoing in early universe galaxies: the ratios between bright central emission and diffuse halo emission are comparable in both redshift regimes, and observational biases such as aperture effects will be similar. As far as Lyα observations can say, the distributions of dust and gas that influence Lyα transport do not evolve strongly.

5.4 Extended Hα: Lyα-haloes produced by in situ recombinations or resonance scattering?

We now focus on the physical origin of the haloes. Is the extended emission produced by scattered radiation, or is it produced by recombining gas at large radii? Since Hα traces the same gas that produces Lyα, we can use our Hα observations to quantify this issue.

The SNR of the Hα data means that we cannot trace it to large radii, which complicates the comparison. Nevertheless, the experiment is interesting, and we therefore perform two component fits to the Lyα profile entirely akin to before, with the one difference that instead of constraining the central component using the FUV data, we now use the Hα data. We find that the difference in quality of the fits is marginal and does not warrant any strong conclusions. Within the uncertainties of the data, the core profile of Lyα can be adequately constrained by both FUV and Hα. However, we do note that in many of the profiles, Hα seems to be slightly more extended than the FUV.

In order to definitively answer whether Lyα is produced by *in situ* recombinations or dominated by scattering, we would require more sensitive or deeper data in Hα that would tell us whether the Hα also shows a break in the profile slope akin to the Lyα and at which relative surface brightness. We have obtained MUSE data for this purpose, and this will be the subject of a forthcoming paper.

Hα emission being extended beyond the ionizing star forming knots may have several important implications for galaxy observations, most notably the escape of ionizing radiation (LyC). LyC emission is now frequently reported in both high- and low-z galaxy samples, where it most strongly correlates with the relative strength of Lyα (Izotov et al. 2018; Steidel et al. 2018; Marchi et al. 2019; Flury et al. 2022). This is intuitive because both UV radiations are absorbed by dust and atomic hydrogen, but a large scatter remains on all these relations.

It is likely that a significant amount of this scatter comes from orientation effects, where LyC measurements are direct line-of-sight estimates, while others (such as Lyα) are the result of reprocessed LyC radiation that has propagated in all directions. These observations show that some Hα is produced outside the stellar knots, and consequently, so is a fraction of the intrinsic Lyα. It is clear, then, that even in the absence of resonance scattering, the path taken by Lyα radiation must necessarily differ from that of the ionizing continuum. Similar arguments can be made about nebular line diagnostics from other species, such as the [O II] and [O III] lines, which are also used as indirect LyC diagnostics. Variations in the extent of these ionized regions are likely a contributing source of the scatter on the Lyα–LyC relations, and a demonstration of how even in compact galaxies at $z \sim 0.25$ (similar to Izotov et al. 2018; Flury et al. 2022) indirect diagnostic information on LyC emission is not produced cospatially with the ionizing radiation.

5.5 Comparison with simulations

Mitchell et al. (2021) investigated a single simulated galaxy and found that emission from the galaxy's ISM, i.e. resonant scattering, dominates the central region but that *in situ* emission from the CGM becomes important around 7–10 kpc. This produces a halo that is qualitatively consistent with both Leclercq et al. (2017) and this work. They also note that around 50 per cent of the CGM emission comes from recombination, which would also naturally produce extended Hα.

Byrohl et al. (2021) examined the relative importance of different source regions for Lyα emission in synthetic galaxies drawn from the TNG50 (Nelson et al. 2019; Pillepich et al. 2019) simulation of IllustrisTNG galaxies. Their synthetic sample spanned a halo-mass range of 10^8 to 10^{12} $M_\odot$, and could well reproduce the light profiles published in Leclercq et al. (2017). The halo masses of our galaxies are of course unknown, but our central surface brightnesses best correspond to the more massive haloes studied by Byrohl et al. (2021) when corrected for cosmological surface brightness dimming. They distinguish between 'intrinsic' and 'processed' Lyα emission, where the former is defined as Lyα that has not undergone scattering outside of the emitting cell, which has a minimum size of 100 pc in the densest regions of the ISM but declines to circumgalactic regions. They found that the intrinsic emission often dominates the centres of their galaxies but drops quickly after around 15 kpc. This is quite consistent with the picture we present here, with a low surface brightness UV emission component tracing the source of Lyα out to larger radii than has been previously observed. Our UV emission drops somewhat faster than Lyα of the galaxies studied in Byrohl et al. (2021), which may be attributable to sample selection effects within the simulations. TNG50 includes galaxies that are larger than the compact galaxies studied here and do not have to compete with observational surface brightness limits.

6 SUMMARY & CONCLUSIONS

We have performed a new Lyα imaging study of galaxies at redshift 0.23–0.31, with a view to accurately measuring the contributions of extended Lyα to the overall output and coupling this to the distribution of ultraviolet stellar light and ionized gas. We have produced Lyα and Hα images for seven compact starbursts that are broadly comparable to those for which similar Lyα studies have been performed at redshifts beyond 3. We now summarize our main findings.

(i) We detect Lyα emission around all galaxies. The average escape fraction of the sample is relatively low compared to distant galaxies, with a mean f_{esc} of 12 per cent, but quite comparable to similar galaxies at low-z (Hayes et al. 2014; Henry et al. 2015).

(ii) The sample appears consistent with other low-z results regarding relations between Lyα output, in terms of EWs, and escape fractions, and properties of the interstellar medium, such as dust reddening and ionization parameter.

(iii) The observed UV sizes and luminosities of our galaxies match the properties of high-redshift galaxies well when measurements are made in comparable ways.

(iv) The observed Lyα to UV size ratio of our sample ranges between 0.8 and 16.9 with a mean of ∼5.6, and the fraction of Lyα that is contributed by the extended emission is 30–90 per cent. While the Lyα to UV size ratio is smaller in our galaxies, the difference between low and high redshifts when also considering the LARS sample is not significant. We therefore conclude that the evidence for evolution between low and high redshift is marginal.

(v) The low-z FUV-continuum data have significantly better intrinsic surface brightness sensitivity than those for galaxies at high-z, which enables us to identify more extended stellar light. However, we find that extending the model above to account for this additional UV component does not significantly impact the halo fraction measurements, indicating that this UV emission comes from an older, less ionizing, stellar population, which does not significantly contribute to the total Lyα emission.

(vi) We are unable to firmly determine whether the Lyα is produced *in situ* or resonantly scattered into the halo. However, we show intriguing hints that Hα is more extended than the central ionizing FUV profile. This could indicate that ionizing radiation is travelling significant distances from the source before being absorbed, implying that ionizing radiation is not entirely confined by the ISM in these galaxies. Further investigation of this with deeper Hα data is underway using VLT/MUSE observations.

ACKNOWLEDGEMENTS

This work is based on observations made with the NASA/ESA *Hubble Space Telescope*, obtained at the Space Telescope Science Institute, which is operated by the Association of Universities for Research in Astronomy, Inc., under NASA contract NAS 5-26555. These observations are associated with program 15643. M.H. is supported by the Knut and Alice Wallenberg Foundation. RA was supported by NASA grant 80NSSC18K110.

DATA AVAILABILITY

The data underlying this article will be shared on reasonable request to the corresponding author.

REFERENCES

Abolfathi B. et al., 2018, ApJS, 235, 42
Bacon R. et al., 2010, in McLean I. S., Ramsay S., Takami H.eds, Proc. SPIE Conf. Ser.Vol. 7735, Ground-based and Airborne Instrumentation for Astronomy III. SPIE,p. 773508,
Baldwin J. A., Phillips M. M., Terlevich R., 1981, PASP, 93, 5
Bik A., Östlin G., Hayes M., Adamo A., Melinder J., Amram P., 2015, A&A, 576, L13
Bohlin R. C., Tsvetanov Z., 2000, Instrument Science Report ACS00–05, Measured throughput and bandpass of the ramp filters. STSCI
Borthakur S. et al., 2015, ApJ, 813, 46
Bridge J. S. et al., 2017, ApJ, 852, 9
Byrohl C. et al., 2021, MNRAS, 506, 5129
Cardelli J. A., Clayton G. C., Mathis J. S., 1989, ApJ, 345, 245
Chen Y. et al., 2021, MNRAS, 508, 19
Daddi E. et al., 2007, ApJ, 670, 156
Diehl S., Statler T. S., 2006, MNRAS, 368, 497
Dijkstra M., 2019, Physics of Ly α Radiative Transfer. Springer, Berlin, Heidelberg
Duval F. et al., 2016, A&A, 587, A77
Elbaz D. et al., 2007, A&A, 468, 33
Erb D. K., Steidel C. C., Chen Y., 2018, ApJ, 862, L10
Feldmeier J. J. et al., 2013, ApJ, 776, 75
Flury S. R. et al., 2022, ApJ, 930, 126
Fruchter A. S., Hook R. N., 2002, PASP, 114, 144
Hayes M., Östlin G., 2006, A&A, 460, 681
Hayes M., Östlin G., Mas-Hesse J. M., Kunth D., Leitherer C., Petrosian A., 2005, A&A, 438, 71
Hayes M., Ostlin G., Atek H., Kunth D., Mas-Hesse J. M., Leitherer C., Jimenez-Bailon E., Adamo A., 2007, MNRAS, 382, 1465
Hayes M., Östlin G., Mas-Hesse J. M., Kunth D., 2009, AJ, 138, 911
Hayes M. et al., 2013, ApJ, 765, L27
Hayes M. et al., 2014, ApJ, 782, 6
Hayes M., Melinder J., Östlin G., Scarlata C., Lehnert M. D., Mannerström-Jansson G., 2016, ApJ, 828, 49
Hayes M. J., Runnholm A., Gronke M., Scarlata C., 2021, ApJ, 908, 36
Hayes M. J., Runnholm A., Scarlata C., Gronke M., Rivera-Thorsen T. E., 2023, MNRAS, 520, 5903
Heckman T., Borthakur S., Wild V., Schiminovich D., Bordoloi R., 2017, ApJ, 846, 151
Henry A., Scarlata C., Martin C. L., Erb D., 2015, ApJ, 809, 19
Izotov Y. I., Schaerer D., Thuan T. X., Worseck G., Guseva N. G., Orlitová I., Verhamme A., 2016, MNRAS, 461, 3683
Izotov Y. I., Worseck G., Schaerer D., Guseva N. G., Thuan T. X., Fricke, Verhamme A., Orlitová I., 2018, MNRAS, 478, 4851
Kauffmann G. et al., 2003, MNRAS, 346, 1055
Kewley L. J., Dopita M. A., Sutherland R. S., Heisler C. A., Trevena J., 2001, ApJ, 556, 121
Krist J. E., Hook R. N., Stoehr F., 2011, in Kahan M. A.ed., SPIE Optical Engineering + Applications. San Diego, California, USA, p. 81270J,
Kunth D., Leitherer C., Mas-Hesse J. M., Ostlin G., Petrosian A., 2003, ApJ, 597, 263
Kusakabe H. et al., 2022, A&A, 660, A44
Laursen P., Duval F., Östlin G., 2013, ApJ, 766, 124
Leclercq F. et al., 2017, A&A, 608, A8
Leclercq F. et al., 2020, A&A, 635, A82
Leitherer C. et al., 1999, ApJS, 123, 3
Luridiana V., Morisset C., Shaw R. A., 2015, A&A, 573, A42
Marchi F. et al., 2019, A&A, 631, A19
Marino R. A. et al., 2013, A&A, 559, A114
Martin C. et al., 2003, in Blades J. C., Siegmund O. H. W.eds, Future EUV/UV and Visible Space Astrophysics Missions and Instrumentation.. SPIE Conference Series,4854, 336
McCully C. et al., 2018, Astropy/Astroscrappy: V1.0.5 Zenodo Release,
Melinder J. et al., 2023, preprint (arXiv:2302.14077)
Mitchell P. D., Blaizot J., Cadiou C., Dubois Y., Garel T., Rosdahl J., 2021, MNRAS, 501, 5757
Momose R. et al., 2014, MNRAS, 442, 110
Momose R. et al., 2016, MNRAS, 457, 2318
Morrissey P. et al., 2018, ApJ, 864, 93
Nelson D. et al., 2019, Comput. Astrophys. Cosmol., 6, 2
Neufeld D. A., 1991, ApJ, 370, L85
Niemeyer M. L. et al., 2022, ApJ, 929, 90
Obreschkow D., Heywood I., Rawlings S., 2011, ApJ, 743, 84
Östlin G., Hayes M., Kunth D., Mas-Hesse J. M., Leitherer C., Petrosian A., Atek H., 2009, AJ, 138, 923
Östlin G. et al., 2014, ApJ, 797, 11
Pillepich A. et al., 2019, MNRAS, 490, 3196
Prevot M. L., Lequeux J., Maurice E., Prevot L., Rocca-Volmerange B., 1984, A&A, 132, 389
Rasekh A. et al., 2021, A&A, 662, A64
Runnholm A., Gronke M., Hayes M., 2021, PASP, 133, 034507
Steidel C. C., Bogosavljević M., Shapley A. E., Kollmeier J. A., Reddy N. A., Erb D. K., Pettini M., 2011, ApJ, 736, 160
Steidel C. C., Bogosavljević M., Shapley A. E., Reddy N. A., Rudie G. C., Pettini M., Trainor R. F., Strom A. L., 2018, ApJ, 869, 123
Tumlinson J. et al., 2013, ApJ, 777, 59
Wisotzki L. et al., 2016, A&A, 587, A98
Yang H., Malhotra S., Rhoads J. E., Leitherer C., Wofford A., Jiang T., Wang J., 2017, ApJ, 838, 4
van Dokkum P. G., 2001, PASP, 113, 1420

This paper has been typeset from a TEX/LATEX file prepared by the author.